HHS Public Access

Author manuscript

*Nat Biomed Eng*. Author manuscript; available in PMC 2023 March 29.

Published in final edited form as:

*Nat Biomed Eng*. 2023 February ; 7(2): 177–191. doi:10.1038/s41551-022-00910-5.

# Aberrant chromatin reorganization in cells from diseased fibrous connective tissue in response to altered chemomechanical cues

**Su-Jin Heo**[1,2,3,4], **Shreyasi Thakur**[5], **Xingyu Chen**[3,6], **Claudia Loebel**[2,3], **Boao Xia**[1,2], **Rowena McBeath**[7], **Jason A. Burdick**[2,3,8], **Vivek B. Shenoy**[2,3,6], **Robert L. Mauck**[1,2,3,4,10], **Melike Lakadamyali**[3,5,9,10]

[1]McKay Orthopaedic Research Laboratory, Department of Orthopaedic Surgery, Perelman School of Medicine, University of Pennsylvania, Philadelphia, PA, USA.

[2]Department of Bioengineering, School of Engineering and Applied Science, University of Pennsylvania, Philadelphia, PA, USA.

[3]Center for Engineering Mechanobiology, University of Pennsylvania, Philadelphia, PA, USA.

[4]Translational Musculoskeletal Research Center, Corporal Michael J. Crescenz VA Medical Center, Philadelphia, PA, USA.

[5]Department of Physiology, Perelman School of Medicine, University of Pennsylvania, Philadelphia, PA, USA.

[6]Department of Materials Science Engineering, School of Engineering and Applied Science, University of Pennsylvania, Philadelphia, PA, USA.

[7]Department of Orthopaedic Surgery, Thomas Jefferson University, Philadelphia, PA, USA.

[8]BioFrontiers Institute and Department of Chemical and Biological Engineering, University of Colorado Boulder, Boulder, CO, USA.

[9]Epigenetics Institute, University of Pennsylvania, Philadelphia, PA, USA.

[10]These authors contributed equally: Robert L. Mauck, Melike Lakadamyali.



**Correspondence and requests for materials** should be addressed to Robert L. Mauck or Melike Lakadamyali. lemauck@pennmedicine.upenn.edu; melikel@pennmedicine.upenn.edu.

Author contributions

S.-J.H., S.T., X.C., C.L., B.X., R.M., J.A.B., V.B.S., R.L.M. and M.L. designed the studies, and analysed and interpreted the data. S.-J.H., S.T., X.C., C.L. and B.X. performed the experiments. S.-J.H., R.L.M. and M.L. drafted the manuscript, and all authors edited the final submission.

Code availability

The custom code for the super-resolution image analysis is available at https://github.com/melikelab/Su-Chin/tree/main/New%20folder.

Competing interests

The authors declare no competing interests.

Additional information

**Extended data** is available for this paper at https://doi.org/10.1038/s41551-022-00910-5.

**Supplementary information** The online version contains supplementary material available at https://doi.org/10.1038/s41551-022-00910-5.

**Peer review information** *Nature Biomedical Engineering* thanks Guanbin Song and the other, anonymous, reviewer(s) for their contribution to the peer review of this work.

## Abstract

Changes in the micro-environment of fibrous connective tissue can lead to alterations in the phenotypes of tissue-resident cells, yet the underlying mechanisms are poorly understood. Here, by visualizing the dynamics of histone spatial reorganization in tenocytes and mesenchymal stromal cells from fibrous tissue of human donors via super-resolution microscopy, we show that physiological and pathological chemomechanical cues can directly regulate the spatial nanoscale organization and density of chromatin in these tissue-resident cell populations. Specifically, changes in substrate stiffness, altered oxygen tension and the presence of inflammatory signals drive chromatin relocalization and compaction into the nuclear boundary, mediated by the activity of the histone methyltransferase EZH2 and an intact cytoskeleton. In healthy cells, chemomechanically triggered changes in the spatial organization and density of chromatin are reversible and can be attenuated by dynamically stiffening the substrate. In diseased human cells, however, the link between mechanical or chemical inputs and chromatin remodelling is abrogated. Our findings suggest that aberrant chromatin organization in fibrous connective tissue may be a hallmark of disease progression that could be leveraged for therapeutic intervention.

Tissue-resident cells (including tissue-resident progenitors) continuously sense changes in their chemophysical micro-environment and use this information to maintain their phenotype and tissue homeostasis[1,2]. Injury or degeneration of load-bearing fibrous connective tissues (such as tendons, ligaments and meniscus) results in changes in tissue structure and mechanics[3–6]. These changes can be seen at the bulk-material level as well as with the emergence of local material microdomains with altered mechanics harbouring cells of aberrant phenotypes[5]. However, it remains unclear whether the altered chemophysical environments in these degenerating tissues drive a change in genome organization that promulgates this aberrant state or whether these changes occur in a cell-autonomous fashion, and this in turn alters the local micro-environment. It is thus essential to elucidate how native cells respond and adapt to their chemophysical environment in order to understand normal physiology and treat pathology in these connective tissues.

Ultimately, phenotypic changes in response to chemophysical cues are linked to the spatial organization of the chromatin in the nucleus, which in turn modulates accessibility and transcriptional activity at specific loci[7–9]. Although our work[10,11] and that of others[9,12–14] demonstrated a clear response in terms of chromatin compaction with changing chemomechanical cues, these visualizations have been somewhat coarse, relying on data acquired at the micrometre-length scale. However, the functional consequences of an altered chromatin spatial organization occur at the nanoscale (in the order of 10–100 nm)[8] and it has been challenging to study this phenomenon using conventional fluorescence microscopy. Although high-throughput chromosome-conformation-capture-based methods have provided valuable information about genome organization, such methods typically require a large population of cells, obscuring cell-to-cell heterogeneity[8,15]. A number of super-resolution microscopy techniques that can overcome the diffraction limitations of conventional microscopy have recently emerged. Super-resolution microscopy (such as stochastic optical reconstruction microscopy (STORM) with a sub-diffraction spatial resolution of approximately 20–30 nm) allows one to address the resolution gap between conventional fluorescence and electron microscopy[8,15,16]. Using this imaging technique,

we recently obtained high-resolution images of the chromatin structure of stem cells at a nanoscale level[8], and demonstrated that this nanoscale chromatin organization is cell-type-specific and nucleosome-enriched regions (termed ‘clutches’) increase in size and density with stem cell differentiation[8]. In addition, recent work using super-resolution microscopy showed that the chromatin nanodomains undergo decompaction and fragmentation in early carcinogenesis, further emphasizing the relevance of higher-order chromatin organization for healthy and disease cell phenotypes[17].

Here, by taking advantage of these recent advances in super-resolution imaging, we determine how chemomechanical changes to the tissue micro-environment during disease regulate the spatial nanoscale chromatin organization. For this, we explored chromatin spatial organization and density of human tenocytes (hTCs) and human mesenchymal stromal cells (hMSCs; that is, human mesenchymal progenitors), and investigated how the spatial organization of chromatin changed in response to physiological and pathological chemophysical cues (such as soft substrates[18] or hypoxic conditions[19]) using super-resolution microscopy. Our findings demonstrate that exogenous chemomechanical perturbations rapidly and reversibly regulate the spatial chromatin organization and localization at the nanoscale level in both healthy hTCs and hMSCs through changes in histone modifications. Furthermore, we found that tendon-degenerative cues altered the nanoscale spatial organization of chromatin and its mechano-responsivity in hTCs. Most notably, when physiological cues were applied to healthy cells, a normal spatial organization and density of chromatin was conferred, whereas diseased hTCs were unable to respond by reorganizing their genome. Collectively, these data support that alterations in the chemophysical environments of fibrous connective tissues with development or degeneration impact nanoscale chromatin organization and may inform new therapeutic strategies for treating pathologies of connective tissue.

## Results

### Tissue degeneration alters the chromatin organization of hTCs.

Tissue degeneration and/or ageing is known to alter the mechanical environment of dense connective tissues, changing both biochemical and biophysical inputs to resident cells, thereby impacting their phenotype[3–5,20]. To determine whether ageing and tissue degeneration drive a change in genome organization, we used super-resolution microscopy and quantitative analysis. We isolated tenocytes from human tendons from three different donors that were: (1) young and healthy (young), (2) young and diagnosed with tendinosis (tendinosis, which is a common tendon pathology associated with repetitive use and mechanical overload[19,21]) or (3) aged and healthy (aged). These hTCs were cultured on glass substrates for 48 h before fixation and super-resolution imaging. The super-resolution images showed that chromatin was distributed throughout the nucleus in young healthy hTC nuclei (Fig. 1a). However, histone H2B (H2B) was unexpectedly primarily localized to the nuclear periphery of the nuclei of young degenerative hTCs (tendinosis; Fig. 1a). To further quantify the chromatin organization in the different cell types, we next used Voronoi tessellation-based image segmentation[8,22]. Voronoi segmentation revealed that H2B localizations clustered to form discrete and spatially separated nanodomains in all cases.

However, analysis of the localization density revealed that the H2B localizations were enriched at the nuclear periphery (defined as 15–20% of the outer area from the nuclear border determined by the image intensity profile across the nucleus) in degenerative hTCs compared with healthy or aged hTCs (Fig. 1a,b and Supplementary Fig. 1a).

Given the dramatic relocalization of chromatin to the nuclear periphery in degenerative hTCs, which is known to contain silenced constitutive heterochromatin[23,24], we next investigated whether the condensation and compaction state of chromatin was different for the different cell types. To address this question, we used a heatmap representation of the super-resolution images based on Voronoi polygon size (Fig. 1c). As the size of Voronoi polygons is inversely proportional to the localization density, smaller polygons represent denser, more compact chromatin (red regions in the heatmap). By placing a threshold on the Voronoi polygon density (inverse of Voronoi polygon size; Supplementary Fig. 1b), we further split chromatin into two compartments: sparse chromatin with low Voronoi density and dense chromatin with high Voronoi density (Supplementary Fig. 1b). Previous work from our group demonstrated that increased transcriptional activity as a result of histone deacetylase (HDAC) inhibition or cell activation corresponds to an increase in sparse chromatin in super-resolution images[8,22,25,26]. In addition, cell types that are known to have a hyper-dynamic and open chromatin, such as embryonic stem cells, also have an increased amount of sparse chromatin in super-resolution images[8]. Finally, inhibition of transcriptional activity leads to an increase in dense chromatin in super-resolution images[27]. These previous results establish a tight link between chromatin density in super-resolution images and the presence of open euchromatin or closed heterochromatin as well as the levels of transcriptional activity. Hence, sparse (or dense) chromatin compartment probably corresponds to open euchromatin (or closed heterochromatin). A heatmap representation of the super-resolution images based on Voronoi polygon size showed an increase in chromatin condensation in degenerative hTCs compared with healthy hTCs (Fig. 1c,d and Supplementary Figs. 1b,c and 2a–c). The changes to the chromatin condensation of degenerative hTCs were distinct from aged hTCs, as the latter contained less condensed H2Bs throughout the nucleus (aged; Fig. 1c,d and Supplementary Figs. 1b,c and 2a–c). This quantification revealed that, compared with healthy hTCs, both sparse and dense chromatin compartments were more compact in diseased hTCs independently of whether the chromatin at the nuclear periphery or interior was analysed. Overall, these data indicate that both tissue degeneration and ageing impact chromatin organization in spatially distinct patterns in hTCs.

### Substrate stiffness alters chromatin organization in hMSCs.

Tissue degeneration alters the chemophysical environment (for example, soft extracellular matrix (ECM))[18] of resident cells—including progenitor cells—which is an important factor in determining cell fate[28,29], and tissues (including tendon tissues) have a wide range of stiffnesses that change with disease[30,31]. We thus hypothesized that the changes in the genome organization of diseased hTCs (or their progenitors) may be driven by aberrant chemomechanical cues in the micro-environment of degenerative tissue and in particular by changes to tissue stiffness. To assess how the physiologically and pathologically relevant biophysical cue impacts genome organization at the nanoscale level, we first

developed a model system using a malleable cell type—that is, hMSCs, progenitor cells that are known to adapt their phenotype in response to substrate stiffness. We used these model cells cultured on substrates of varying stiffness to both optimize quantitative super-resolution imaging of chromatin and visualize changes to genome organization in response to biophysical cues. To do this, hMSCs were plated on chambered cover glass (glass; approximately 70 GPa), 30 kPa (stiff) or 3 kPa (soft) methacrylated hyaluronic acid (MeHA) hydrogels modified with RGD to promote cell adhesion[32], followed by 2 d of culture in basal cell growth medium. Super-resolution images of H2B provided a genome-wide view of chromatin organization in the nuclei of hMSCs cultured on these substrates (Fig. 2a). These images once again revealed histone nanodomains, which could not be observed with conventional microscopy[8,19]. Although H2B localizations clustered to form discrete and spatially separated nanodomains in hMSC nuclei on all three substrates, these domains were distributed more evenly throughout the nucleus on glass and stiff substrates compared with soft substrates (Fig. 2a). Notably, the H2B nanodomains were mainly sequestered at the nuclear periphery on soft substrates, resembling the organization we observed in degenerative hTCs (Fig. 1a). Analysis of the localization density revealed that the H2B localizations were enriched at the nuclear periphery on soft substrates compared with stiff or glass substrates (Fig. 2a,b). These changes in H2B localization were not due to changes in nuclear shape, as cells cultured on different substrates had a small change in nuclear volume and similarly the total number of localizations of H2B per nuclear area (Supplementary Fig. 3a,b). Hence, these results suggest that chromatin undergoes spatial reorganization in response to substrate stiffness. The H2B heatmaps also showed visual differences in how the condensed chromatin (red in Fig. 2c) was distributed throughout the nucleus on the different substrates. In particular, dense chromatin was somewhat enriched at the nuclear periphery but also localized throughout the hMSC nucleus on glass substrates (Fig. 2c,d and Supplementary Figs. 4a,b and 5a–c). Conversely, dense chromatin was highly enriched at the nuclear periphery on soft substrates. Compared with glass, both sparse and dense chromatin compartments were less compact on stiff substrates. Interestingly, on soft substrates, both chromatin compartments underwent re-compaction to almost the same level as on the glass substrate (Fig. 2c,d and Supplementary Figs. 4a,b and 5a–c). Together, these data suggest that substrate stiffness regulates nanoscale chromatin spatial organization and compaction in hMSCs.

### Substrate stiffness alters the histone methylation levels of hMSCs.

Histone post-translational modifications play crucial roles in the regulation of gene activation and repression[33–35], and different modifications correlate with open or closed chromatin. In particular, H3 lysine 4 trimethylation (H3K4me3) is a marker of active euchromatin, whereas histone H3 lysine 27 trimethylation (H3K27me3) is associated with heterochromatin and gene repression[36,37]. Having established that substrate stiffness alters chromatin organization and condensation in hMSCs, we next investigated whether substrate stiffness also leads to changes in the localization and condensation state of active chromatin marked with H3K4me3 and repressed chromatin marked with H3K27me3. We thus labelled hMSCs with antibodies to these two specific histone modifications and obtained super-resolution images under the three substrate conditions. Heatmaps of H3K4me3 and quantitative analyses showed that, compared with hMSCs cultured on glass substrates, the

levels of H3K4me3 were slightly increased in hMSCs cultured on stiff substrates, whereas these levels were significantly lower in hMSCs cultured on the soft substrates (Fig. 3a,b). These data are consistent with the H2B condensation analysis described earlier and suggest that loss of active histone marks correlates with increased chromatin condensation on soft substrates (Fig. 2). Conversely, the amount of H3K27me3 was lower on stiff substrates (in particular, at the nuclear interior) and enhanced on soft substrates (particularly at the nuclear periphery) compared with glass substrates (Fig. 3c,d). These results indicate that increased peripheral chromatin localization and increased chromatin condensation on soft substrates is further correlated with increased levels of H3K27me3, suggesting that soft substrates may lead to gene suppression (Fig. 2).

Having observed that substrate stiffness regulates chromatin organization at the nanoscale and that substrate-dependent chromatin remodelling correlates with changes in the levels of histone methylation marks, we next investigated the role of the methyltransferase Enhancer of zeste homologue 2 (EZH2, which catalyses H3K27me3)[38,39] in substrate-stiffness-mediated chromatin reorganization in hMSCs. To do this, we used GSK343, a selective inhibitor of EZH2 (refs. [40,41]) to treat hMSCs during the culture period, as we found that the levels of EZH2 were increased in the nuclei of hMSCs cultured on soft substrates (Supplementary Fig. 6). H2B STORM images, heatmaps and quantitative Voronoi analyses revealed that EZH2 inhibition did not substantially alter the spatial organization of H2B under stiff or glass substrates, and only led to a slight decondensation of both sparse and dense chromatin compartments (glass and stiff; Fig. 3e,g and Supplementary Figs. 7 and 8). On the other hand, EZH2 inhibition decreased the enrichment of chromatin at the nuclear periphery of cells cultured on soft substrates (Fig. 3e,f) and led to a substantial decondensation of both sparse and condensed chromatin compartments (Fig. 3e,g and Supplementary Figs. 7 and 8). Conversely, when lysophosphatidic acid (a G-protein agonist that increases cellular contractility[42,43]) was applied, we observed increases in the condensation state of both sparse and condensed chromatin compartments on all substrates, with the most prominent changes observed in the nuclei of hMSCs on soft substrates (Supplementary Figs. 9 and 10). These data suggest that altered physical forces and cellular contractility on soft substrates may play important roles in chromatin translocation to the nuclear periphery in hMSCs. Overall, our results indicate that substrate stiffness regulates the nanoscale spatial organization and condensation of chromatin through changes in cellular contractility and alterations of the histone methylation status in hMSCs (Fig. 3h).

### Prediction of chromatin remodelling.

The formation of heterochromatin has previously been proposed to be a result of several mechanisms, including liquid–liquid phase separation of chromatin and chromatin-associated proteins like HP1α, neutralization of electrostatic charges by linker histone H1 and transcriptional silencing. As noted earlier, specific epigenetic marks are known to correlate with condensed heterochromatin or open euchromatin. However, the effects of epigenetic regulators on chromatin organization are not fully understood and it is unknown whether the kinetics of acetylation and methylation can alter chromatin condensation. To explore these points and determine whether the observed impact of substrate stiffness on chromatin condensation is the result of the changes in histone methylation status,

we developed a phase-field model that simulates heterochromatin formation (Fig. 4a, 'Model development' in Supplementary Information, Supplementary Figs. 11–13 and Supplementary Table 1). This model incorporates the kinetics of methylation and acetylation (mediated by epigenetic regulators in a substrate-stiffness-dependent manner) and interactions of chromatin with nuclear lamina to predict the spatial distribution and volume fraction of heterochromatin.

The key features in our model include the energetics of the chromatin–chromatin and chromatin–lamina interactions specified in equation (1), and the kinetics of chromatin diffusion and chemical reactions described in equations (3) and (4) (Fig. 4a). Our model indicates that these two inputs impact the organization of chromatin in different ways. The energetic contributions alone drive the change in the nanodomain distribution of heterochromatin into a single large cluster to minimize interfacial energy (known as Ostwald ripening[44]). On the other hand, the methylation and acetylation reactions result in interconversion of the eu- and heterochromatin phases, resulting in the formation of more interfaces. Faster reactions (higher rate of methylation, $\Gamma_{me}$ or acetylation, $\Gamma_{ac}$) would thus result in a larger interface area, which competes with the coarsening behaviour that minimizes the interfacial energy. Thus, our simulations reveal that the methylation and acetylation reactions suppress the Ostwald ripening, leading to an optimal size of heterochromatin domains (Fig. 4a). Note that our model is independent of any assumptions on the specific molecular origins of the chromatin–chromatin and chromatin–lamina interactions. The energetic parameters (Methods) incorporate the energy associated with the chromatin–chromatin interactions in the euchromatin and heterochromatin phases. Specific molecular mechanisms such as chromatin crosslinking by HP1α and/or linker histone H1-mediated reduction in histone–histone repulsion resulting in heterochromatin formation can be incorporated in the values of the energetic interaction parameters.

This theoretical model agrees with our experimental observations of dense chromatin-rich nanodomains that are stable against coarsening. Furthermore, through our simulations we found that the phase-separated heterochromatin clusters transform from round to lamellar morphologies with increasing levels of methylation (Fig. 4a) and the size of the heterochromatin clusters increase with the level of methylation (Fig. 4b, refer to section 1 of Model development' in Supplementary Information for derivation of the scaling relation). In agreement with this prediction, we observed larger dense chromatin clusters when cells were cultured on soft substrates, where we also identified increased levels of methylation (Fig. 4d). Finally, the enzymatic reactions also influence the balance between the chromatin–chromatin and chromatin–lamina interactions. Our simulation predicted that more heterochromatin localizes to the nuclear lamina as the level of methylation increases (Fig. 4a), consistent with our experimental observations on soft substrates (Fig. 4d). The thickness of heterochromatin at the nuclear border also scaled with the methylation levels (Fig. 4c, refer to section 2 of Model development in Supplementary Information for derivation of the scaling relation). Our model was also able to accurately predict the decreased localization of chromatin at the nuclear border following GSK343 inhibition of EZH2 (Fig. 4e), which leads to decreased levels of methylation.

Overall, our model recapitulates the experimental results on how substrate-dependent changes in the histone methylation levels impact the spatial organization of chromatin in the nucleus and provides support that the levels of acetylation and methylation compete with phase separation and have a direct bearing on chromatin organization.

### Chromatin reorganizes rapidly with dynamic mechanical cues.

The data presented so far indicated that substrate stiffness alters chromatin organization and localization via impacts on cell contractility and downstream methyltransferase activity, but such static time-invariant mechanical cues do not replicate the dynamic and time-varying characteristics of remodelling within actively loaded cellular environments. Hence, we next investigated how dynamic alterations to the biophysical environment impact nanoscale chromatin organization in hMSC nuclei. We used an in situ substrate-stiffening[45,46] system to evaluate changes in H2B nanoscale spatial organization and chromatin condensation in hMSCs. Cells were cultured on a ‘stiffening hydrogel’ system that provided a rapid change in substrate stiffness from a soft (approximately 3 kPa) to a stiff (approximately 30 kPa) mechanical state (Fig. 5a)[45]. This stiffening hydrogel system has previously been characterized[45,46] and the change in substrate stiffness is mediated by a secondary crosslinking reaction that occurs over the course of several minutes[45,46]. Consistent with our previous results[45], hMSCs responded to stiffening immediately with increases in cell area (Supplementary Fig. 15a). As observed in the static soft substrates (3 kPa), heatmaps of H2B density revealed that chromatin was primarily localized to the nuclear periphery for the first 6 h after stiffening (Fig. 5a,b), followed by a continual redistribution from the nuclear periphery to the nuclear interior between 6 and 48 h after stiffening (Fig. 5a,b). These changes in the spatial organization of chromatin were accompanied by a continual decrease in the condensation state of both sparse and dense chromatin compartments (Fig. 5c and Supplementary Fig. 15b). Interestingly, changes in condensation started at 2 h after stiffening and hence preceded the changes in spatial organization, suggesting that the decondensation of chromatin probably leads to its spatial remodelling in the nucleus. The amount of decondensation reached a plateau at around 60% of the starting value by 18 h after stiffening (Fig. 5c and Supplementary Fig. 15b) and lasted up to day 7 (Supplementary Fig. 16a,b).

In a previous study we demonstrated that substrate stiffening increased actomyosin-driven contractility of hMSCs within approximately 4 h (ref. [45]); we thus next examined the roles of actomyosin-driven contractility in chromatin organization and condensation in response to substrate stiffening. We obtained super-resolution images of H2B in hMSCs cultured on the stiffening MeHA system with or without treatment with Y27632 (Y27; a ROCK inhibitor) before substrate stiffening. Consistent with our findings, control hMSCs (without Y27 treatment) altered their spatial organization of chromatin and underwent chromatin decondensation within 6 h, whereas the Y27 treatment blocked this substrate-stiffening-mediated chromatin remodelling (Fig. 5d,e and Supplementary Fig. 17a,b). These data indicate that ECM-stiffening-mediated chromatin decondensation and redistribution from the border to the inside of the hMSC nucleus requires actomyosin-based cellular contractility (Fig. 5f).

Changes in micro-environmental stiffness represent just one in vivo physical cue that may regulate cell function. To determine whether other dynamic physical cues also regulate chromatin nano-organization, we also investigated the effects of fluid-flow induced shear stress (FSS). For this, a custom-made polydimethylsiloxan (PDMS) microfluidic chamber was developed to impose FSS to hMSCs seeded on glass substrates with varying magnitudes (1–5 dyne $cm^{-2}$) and durations (0.5–2 h; Extended Data Fig. 1a). FSS resulted in changes in chromatin distribution with increases in the total number of H2B localizations at the nuclear periphery and changes in chromatin condensation throughout the nucleus (Extended Data Fig. 1b,c). Heatmaps of H2B density and quantitative analyses indicated that FSS applied at 1 dyne $cm^{-2}$ for 30 min or 2 h resulted in marked chromatin condensation (Extended Data Fig. 1b,d,e). Conversely, higher magnitude FSS (5 dyne $cm^{-2}$) applied for a short duration (0.5 h) decreased chromatin condensation (control; Extended Data Fig. 1b,d,e). Together, these data suggest that dynamic biophysical perturbations regulate nanoscale chromatin organization in a complex and rapid manner in the nuclei of hMSCs.

### ‘Degenerative’ cues alter the chromatin organization of hTCs.

Given our results on the impact of biophysical cues on the nanoscale chromatin organization in vitro, we next addressed our initial hypothesis that cues from the degenerative chemophysical environment (for example, soft ECM[18], hypoxia[19] and inflammation[47]) might result in nanoscale chromatin remodelling and cause young healthy hTCs to take on features that are comparable to that seen in aged or degenerative (tendinosis) hTCs. To test this hypothesis, we first cultured hTCs isolated from young healthy donors on glass, stiff (30 kPa) or soft (3 kPa) substrates for 2 d in basal growth medium[4,9]. Super-resolution heatmaps once again revealed H2B localizations that were clustered to form distinct H2B nanodomains in the nuclei of young healthy hTCs cultured on glass substrates (Fig. 6a). Interestingly, when these young hTCs were cultured on stiff substrates, chromatin condensation for both sparse and condensed chromatin compartments decreased throughout the nucleus, reaching levels similar to that seen in the aged hTCs cultured on glass (Fig. 6a,b). Notably, chromatin was primarily relocalized to the nuclear periphery on soft substrates, comparable to that seen in degenerative hTCs (tendinosis; Fig. 6a,b). Chromatin also became more condensed, in particular in the nuclear interior (Fig. 6a and Extended Data Fig. 2a,b). Interestingly, the chromatin condensation at the nuclear border decreased for hTCs cultured on soft substrates (Extended Data Fig. 2a,b), unlike the increased condensation seen for degenerative hTCs (Fig. 1d,e), suggesting that disruption of the mechanical micro-environment alone is not sufficient to fully explain the chromatin remodelling seen in degenerative hTCs and additional factors are at play. Overall, these data suggest that altered mechanical properties of tissues with tendon ageing or microdamage may drive some of the aberrant changes to the nanoscale organization of chromatin in disease.

Next, we investigated how changes in oxygen tension impact chromatin organization in young healthy hTCs given that previous studies have shown that oxygen levels are altered in degenerative tissues and that hypoxia is a critical regulator of early human tendinopathy[19,48,49]. We seeded young healthy hTCs on glass substrates for 1 d, followed by 4 d of culture under normoxic (21% $O_2$) or hypoxic (1% $O_2$) conditions. Degenerative

hTCs (tentinosis) cultured under normoxia maintained an altered chromatin state consisting of increased chromatin condensation and localization at the nuclear periphery compared with healthy hTCs (young) cultured under normoxia (Fig. 6c,d and Extended Data Fig. 2c,d). Interestingly, when healthy hTCs were cultured under the hypoxic culture conditions, their chromatin relocalized to the nuclear periphery and underwent increased condensation, similar to that seen in tendinosis hTCs (Fig. 6c,d and Extended Data Fig. 2c,d). These results suggest that, similar to altered mechanical cues, the altered oxygen tension present in tendon tissues as a consequence of injury or degeneration leads to aberrant chromatin remodelling in hTCs.

Finally, we investigated how inflammatory cytokines (for example, interleukin 1β (IL-1β) and tumour necrosis factor-α (TNF-α)) impact the nanoscale chromatin organization of young healthy hTCs because injury and ageing are also associated with increased levels of inflammation. These pro-inflammatory cytokines are secreted from immune cells that promote tendon inflammation processes in early tendon repair[50,51]. We cultured young hTCs on glass substrates for 1 d, followed by additional culture for 24 h with or without exposure to IL-1β (0.1 or 1 ng $ml^{-1}$) or TNF-α (1 or 10 ng $ml^{-1}$). As observed in tendinopathic nuclei, treatment with pro-inflammatory cytokines resulted in the reorganization of chromatin to the nuclear periphery and increased chromatin condensation in young healthy hTCs (Fig. 6e,f and Extended Data Fig. 2e,f). In the case of TNF-α, the magnitude of the observed changes in chromatin organization and condensation was dose-dependent and treatment with a higher concentration (10 ng $ml^{-1}$) led to more profound changes compared with treatment with a lower concentration (1 ng $ml^{-1}$). Interestingly, the extent of the changes in the spatial organization and condensation of chromatin was largest in cells cultured on soft substrates or under hypoxic conditions, with inflammatory cytokines contributing to a lesser extent to the relocalization and condensation of the peripheral chromatin. Together, these data support that changes in the chemophysical environment associated with tissue injury or degeneration collectively impact chromatin organization in hTCs and may instigate the phenotypic changes characteristic of loss of resident-cell function.

### Degeneration impacts mechanical sensitivity of hTCs.

Given that hTCs rapidly respond to changes in their mechanical environments with alterations in the spatial organization and condensation of chromatin, we finally examined how tissue degeneration or ageing impacts their mechanical sensitivity. For this, young, tendinosis and aged hTCs were seeded onto the stiffening hydrogel system and pre-cultured for 24 h, followed by an additional 24 h of culture after stiffening. Samples were then fixed to observe chromatin organization at the nanoscale level. In agreement with what was observed on soft substrates, H2B in young, tendinosis and aged hTCs was primarily localized to the nuclear periphery within 4 h after stiffening (Fig. 7a). Following 24 h of stiffening, the chromatin in young hTCs became more uniformly dispersed and de-compacted throughout the nucleus (Fig. 7a–c). Aged cells responded with the same trend to the increase in substrate stiffness but to a lesser extent in terms of chromatin decondensation (Fig. 7a–c). However, when the tendinopathic cells were cultured on the stiffening hydrogels, no change in the spatial organization of the chromatin was observed

(Fig. 7a–c) and the extent of chromatin decompaction, particularly at the nuclear periphery, was substantially lower compared with young and aged cells (Fig. 7a–c). These data suggest that the prolonged alterations in nanoscale chromatin organization in hTCs may be associated with a loss of mechanical sensitivity with degeneration.

## Discussion

In this work, we used super-resolution microscopy to show that the nanoscale organization of chromatin in the nucleus of healthy fibrous tissue and progenitor cells is highly responsive to mechanical perturbations, and that this responsivity depends on a patent cytoskeletal network and dynamic changes in histone modifications (Fig. 8). It has been shown that progenitor cells (hMSCs) can be differentiated into different cell lineages by changing the substrate stiffness[28]. Our previous work also demonstrated that hMSC differentiation into fibrochondrogenic cells following treatment with soluble factors or the application of dynamic tensile loading is accompanied by increased chromatin condensation[11]. In addition, we demonstrated that chromatin organization visualized by super-resolution microscopy is cell-type-specific and that chromatin undergoes remodelling during differentiation and reprogramming[8]. Together, these results suggest that chromatin remodelling and cell differentiation go hand-in-hand and the changes to the spatial organization of chromatin that we observed in hMSCs under different substrate-stiffness conditions may be a cause or consequence of hMSC differentiation into different cell lineages. Future work will dissect the causes and consequences linking chromatin remodelling and cell differentiation. Importantly, we also showed that when degenerative tissue-resident cells are exposed to dynamic mechanical environments that restore physiological chromatin spatial organization in healthy cells, these diseased cells are unresponsive. This suggests that when cells are in a diseased state, their chromatin organization may undergo a permanent change. This lack of mechano-responsivity in degenerative cells may indicate that the cells in these tissues will fail to resume their normal functionality even if surgical and/or rehabilitative approaches are applied. This would have important implications for how and when clinical therapies are applied to treat human disease.

The appreciation of potential plastic remodelling in the chromatin of diseased cells arose from a comprehensive analysis of the response of tendon cells to physiological cues. Given that tissue development and degeneration alter the biophysical properties of connective tissues[3–5], we investigated how tissue development or degeneration impacts chromatin organization in tissue-resident cells (that is, hTCs from tendon). Interestingly, our data show that tissue ageing (which increases tissue stiffness[52,53]) decreases chromatin condensation in hTCs, whereas degeneration (which decreases local tissue stiffness[30,54]) increases chromatin condensation and leads to the relocalization of condensed chromatin to the nuclear periphery. Furthermore, when healthy young hTCs were exposed to degenerative chemophysical environments—including low substrate stiffness[30,54], low oxygen tension (which is altered with tissue injury and is critical in early tendinopathy[19,48,49]) and inflammation[50,51]—this bias in chromatin localization to the nuclear periphery was increased, similar to how chromatin is organized in the nucleus of degenerative hTCs from tendinosis patients. Pro-inflammatory cytokines such as IL-1β and TNF-α are mainly

involved in the inflammation processes[50,51], which take place in patients with acute tendon injury[55,56], suggesting that the aberrant chromatin remodelling events we observed in hTCs from patients with chronic degeneration may also occur in shorter time scales after acute injury. It would be interesting to dissect the impact of acute versus chronic injury on the spatial organization and density of the chromatin of hTCs in future studies. Aberrant chromatin reorganization is also associated with many diseases, which leads to defects in gene regulation resulting in pathological gene expression programmes[57–60] and abnormal protein/matrix production of the cells. Our findings suggest that altered cellular micro-environments during development or degeneration, perhaps as a result of microscale damage and altered local chemophysical environments, could lead to aberrant and persistent genome reorganization and differentiation of endogenous progenitor cells residing in the tissues. Given that degenerative cells that were exposed to dynamic mechanical environments that restore physiological spatial organization of chromatin in healthy cells remained unresponsive, this may further suggest that there is a ‘mechano-epigenetic memory’ in these diseased cells, which could limit the resolution of the diseased phenotype with therapy. It would be interesting to determine the timing of when the epigenetic memory is lost following acute injury to further guide the timing of therapeutic intervention in future studies.

Using this same super-resolution microscopy approach coupled with custom dynamic substrates, we also queried the time-dependent changes and mechanisms by which chromatin remodels in response to biophysical inputs. Specifically, we showed that substrate stiffness regulates both the spatial organization and the condensation state of chromatin at the nanoscale level, with stiff substrates resulting in less condensed chromatin and increased H3K4me3 nanodomains in human mesenchymal progenitors. Notably, these nanodomains were distributed throughout the hMSC nuclei when compared with their localization on soft substrates. Given that such epigenetic marks and physical distribution is associated with active chromatin, these data suggested that stiff substrates may enhance the overall transcriptional activation of these cells. Conversely, when these same cells were placed on soft substrates, highly condensed chromatin domains relocalized to the nuclear periphery, a region in which constitutive heterochromatin resides and methyltransferases are abundant[23,61]. This nuclear periphery has long been considered as a transcriptionally repressive area[62] where inner nuclear membrane proteins in the nuclear lamina interact with proximal chromatin creating heterochromatin structures[63,64]. It has recently been suggested that this laminal sequestration at the nuclear envelope depends on specific epigenetic modifications and indeed we observed that hMSCs on soft substrates increased their nanoscale H3K27me3 localization at the nuclear periphery. Notably, when the activity of EZH2 (a selective inhibitor of histone H3K27 methyltransferase) was inhibited, these spatial and epigenetic changes were prevented, even on soft substrates. These data indicate that soft substrates cause chromatin condensation and chromatin localization primarily to the nuclear periphery, and that this is mediated by EZH2, probably resulting in genome-wide transcriptional suppression.

This study shows that fibrous connective tissue degeneration or degenerative chemophysical cues cause global nanoscale chromatin reorganization. However, a central question that remains unanswered in both degenerative and progenitor cells is what specific genetic

loci move to the periphery and the consequences of these spatial reorganization events on the transcriptional activity of such loci during degeneration and differentiation. Given the massive chromatin relocalization and condensation that we observed in degenerative hTCs, it is probable that the effects are genome-wide and not restricted to a few specific genomic regions. In addition, given that histone modifications govern chromatin organization, which is mediated by specific enzyme activities (such as histone methyltransferases or histone acetyltransferases), small-molecule epigenetic modifiers may be considered to restore healthy chromatin structure and gene expression in degenerative cells to improve the repair of connective tissue. Future work in this area should employ such strategies, with a specific focus on targeting key loci that are critical for tissue function and regeneration in vivo as well as on identification of the timing over which such interventions might be therapeutically viable (that is, before the modification events result in a plastic remodelling of the chromatin to a diseased configuration).

Overall, these findings expand our knowledge of the link between biophysical and chemical micro-environment and genome organization, and may open the door to the identification of epigenetic modifiers that promote the recovery of a healthy chromatin structure in degenerative hTCs to improve the regeneration of native fibrous connective tissue. The findings may also help advance diagnostic and therapeutic approaches and regenerative-medicine strategies for the repair of dense connective tissue.

## Methods

### Preparation of cells.

Established protocols were used to isolate hTCs from human finger flexor tendon tissues[19,65]. Human tendon was obtained from patients undergoing revision amputation for traumatic hand injury who were young (36 and 42 yr), aged (60 and 81 yr) or had been diagnosed with tendinosis (35 and 39 yr) using IRB-approved protocols (#13D.238). Briefly, human tendon tissues (2 × 2 mm) were digested in collagenase solution and the digested tissues were centrifuged. The cell pellets were resuspended and plated in basal growth medium (high glucose DMEM medium, 10% penicillin–streptomycin, l-glutamine and 10% fetal bovine serum (FBS)). Experiments were performed using hTCs of early passage (less than or equal to passage 6).

Human MSCs were isolated from fresh bone marrow from human donors (Lonza; male, 23 yr; female, 18 yr; and male, 22 yr) as reported previously[66,67]. Briefly, using Ficoll density gradient centrifugation (300g; 20 min), bone marrow was separated to obtain mononuclear cells, which were then plated and expanded on tissue-culture plastic in α-modified essential medium (α-MEM, 10% FBS, 1% penicillin–streptomycin and 5 ng $ml^{-1}$ basic fibroblast growth factor) at 37 °C and 5% $CO_2$ until the colonies reached 80% confluency and then stored in liquid nitrogen (95% FBS and 5% dimethylsulfoxide). All hMSCs were expanded in standard growth medium (α-MEM, 10% FBS and 1% penicillin–streptomycin).

### Synthesis of MeHA.

MeHA was synthesized as described previously[32,68,69]. Briefly, sodium hyaluronate (Lifecore; approximately 74 kDa) was dissolved in deionized water (2% (wt/vol)) and adjusted to pH 9.5 with the addition of 1 M NaOH, followed by the addition of methacrylic anhydride (2.8 ml $g^{-1}$ hyaluronic acid). The reaction was allowed to proceed for 4 h on ice, while maintaining pH 9.5, followed by a second addition of methacrylic anhydride (2.8 ml $g^{-1}$ hyaluronic acid) for 4 h at pH 9.5. The polymer was purified via dialysis, lyophilized and modification of approximately 100% confirmed using $^{1}$H NMR.

### Fabrication and stiffening of MeHA films.

To obtain MeHA hydrogel films (6% (wt/vol)) with an elastic modulus of approximately 3 kPa (soft), MeHA was prepared using Michael-type addition crosslinking with dithiothreitol (0.97 mM) in PBS containing 0.2 M triethanolamine at pH 9)[32]. Hydrogel precursor solution containing thiolated RGD peptide (1 mM) was pipetted onto coverslips functionalized with 3-(trimethoxysilyl)propyl methacrylate and incubated for 30 min at 37 °C to obtain a crosslinked hydrogel film that was approximately 15 μm thick[32]. To generate stiffening hydrogels with an elastic modulus of approximately 30 kPa, soft hydrogel films were incubated in 0.05% lithium acylphosphinate in PBS for 30 min at 37 °C, followed by exposure to blue light (400–500 nm; 10 mW $cm^{-2}$) for 5 min (refs. [45,46]). Stiff hydrogels (approximately 30 kPa) were fabricated by exposing hydrogel precursor solutions in PBS containing 1 mM RGD and 0.05% lithium acylphosphinate to blue light (400–500 nm; 10 mW $cm^{-2}$) for 3 min. For nuclear-volume measurements, three-dimensional *z*-stack confocal 4,6-diamidino-2-phenylindole images were analysed using the Volocity software (Improvision Inc.).

### Theoretical modelling.

In our modelling approach, the volume fractions of euchromatin, heterochromatin and nucleoplasm that depend on the location **x** and time $t$ are defined as $\phi_e(\mathbf{x},t)$, $\phi_h(\mathbf{x},t)$ and $\phi_n(\mathbf{x},t)$ respectively, such that $\phi_e + \phi_h + \phi_n = 1$. Motivated by the experimental H2B density maps (Fig. 3e,f), we considered chromatin as phase-separating into (1) a euchromatin-rich phase and (2) a heterochromatin-rich phase in the nucleus. Each of these phases contain different amounts of nucleoplasm. We constructed a free-energy density[70–72], $f$, as a function of volume fractions $\phi_h$ and $\phi_e$

$$f(\phi_e,\phi_h) = \underbrace{\frac{a}{2}\phi_e^2 + \frac{b}{2}(\phi_h-\psi)^2\phi_h^2}_{\text{chromatin-chromatin interactions}} + \underbrace{c\phi_h e^{-d/d_0}}_{\text{chromatin-lamina interactions}} \quad (1)$$

where the parameters $a$ and $b$ characterize the entropic contribution and enthalpy, arising from chromatin–chromatin interactions. The double well defined by the second term captures the separation of chromatin into two phases, a heterochromatin-rich phase with $\phi_h = \psi$ and a euchromatin-rich phase with $\phi_h \sim 0$. Molecular mechanisms of formation of heterochromatin can be incorporated in the values of the energetic interaction parameters $a$ and $b$. For example, the presence of HP1α that chemically crosslinks chromatin to chromatin can be captured by varying the parameter $b$. Furthermore, the increased chromatin

compaction in the heterochromatin domain may additionally be captured by increasing the volume fraction $\psi$ of the heterochromatin in the condensed phase. The last term captures interactions between heterochromatin and nuclear lamina, which gradually vanish over a length scale, $d_0$, when the distance to the nuclear lamina $d$ increases. The parameter $c < 0$ characterizes the strength of the chromatin–lamina interactions, with a preference for the heterochromatic phase at the lamina, as suggested by previous studies[73–75]. The total free energy of the system can then be written as

$$F = \int \left[ f(\phi_h) + \frac{\gamma'}{2}(\nabla \phi_e)^2 + \frac{\gamma}{2}(\nabla \phi_h)^2 \right] d\Omega \tag{2}$$

where the integral is over the volume of the nucleus Ω. The terms proportional to $\gamma$ and $\gamma'$ in the integrand penalize strong gradients of $\phi_h$ and $\phi_e$, which correspond to the energy of the interface between the heterochromatic and euchromatic phases (section 1 of Model development in Supplementary Information).

The temporal evolution of the two phases of chromatin is governed by diffusion in response to the gradients in the chemical potential of eu- and heterochromatin $\left(\frac{\delta F}{\delta \phi_i}, i = e, h\right)$ as well as the interconversion of the two phases due to methylation and acetylation regulated by epigenetic factors (Fig. 3a). The evolution equations can be written as[72,76,77]

$$\frac{\partial \phi_h}{\partial t} = \underbrace{m_h \nabla^2 \frac{\delta F}{\delta \phi_h}}_{\text{diffusion}} + \underbrace{\Gamma_{me}\phi_e - \Gamma_{ac}\phi_h}_{\text{epigenetic}} \text{regulation} \tag{3}$$

$$\frac{\partial \phi_e}{\partial t} = \underbrace{m_e \nabla^2 \frac{\delta F}{\delta \phi_e}}_{\text{diffusion}} - \underbrace{\Gamma_{me}\phi_e + \Gamma_{ac}\phi_h}_{\text{epigenetic}} \text{regulation} \tag{4}$$

Here $m_h$ and $m_e$ denote mobilities of heterochromatin and euchromatin. Note that while diffusion kinetics alone would individually conserve the total amount of heterochromatin and euchromatin in the nucleus, methylation and acetylation reactions allow conversion of euchromatin into heterochromatin and vice versa. For simplicity, we assume both acetylation and methylation follow first-order kinetics, although the terms can be made as complicated as needed. We use $\Gamma_{me}$ and $\Gamma_{ac}$ to denote the rates of methylation and acetylation, respectively. These two terms can capture the impact of the down (or up)-regulation of enzymes such as HDACs or histone acetyl transferases that facilitate the switch in epigenetic states[29,78]. We set up the simulation to numerically solve equations 3 and 4 with the parameters specified in Supplementary Table 1. We introduced small perturbations to $\phi_h$ and $\phi_e$ around their initial values to initiate the separation of chromatin into the two phases and let the simulation proceed until a steady state was reached.

### Fabrication of the microfluidic chamber.

To apply fluid-induced shear stress, a microfluidic chamber system was developed. For this, a silicone elastomer base (Sylgard 184 PDMS) and curing agent were mixed thoroughly

at a ratio of 10:1 (wt/wt) and the mixture was then degassed in a vacuum chamber at room temperature for 10 min. The cleared mixture was poured over three-dimensional printed patterned acrylic masters (microfluidic channel dimensions: 5 mm (width) × 0.5 mm (height) × 20 mm (length)) sitting on a petri dish. The device was cleared of bubbles and cured at 80 °C for 1 h. The PDMS moulds were separated from the petri dish and the masters, and isolated from each other using a craft knife. The edges of the PDMS casts were chamfered to ensure exact flush between the cast surface and the coverslip glass. The inlet and outlet were drilled with a biopsy punch (diameter of 1 mm), concentric with the inlet and the outlet reservoirs. A thin layer of non-cured PDMS and curing agent mixture was applied around the microfluidic channel and a coverslip glass was gently attached onto the bottom of the cast. The assembled chambers were left to cure overnight at room temperature before use.

### STORM imaging and analysis.

For STORM imaging, cells were fixed in methanol–ethanol (1:1) at −20 °C for 6 min, followed by incubation in blocking buffer containing 10% (wt/vol) BSA (Sigma) in PBS for 1 h as previously described[8]. The samples were incubated overnight with rabbit anti-H2B (1:50; Proteintech, 15857–1-AP), rabbit anti-H3K4me3 (1:100; Thermo, MA5–11199) or rabbit anti-H3K27me3 (1:100; Thermo, PA5–31817) at 4 °C. After repeated washing in PBS, the samples were incubated with secondary antibodies custom labelled with activator–reporter dye pairs (Alexa Fluor 405 (A30000)–Alexa Fluor 647 (A20006), Invitrogen) for STORM imaging as previously described[8]. All images were taken using a commercial STORM microscope system from ONI (Nanoimager S) fitted with a ×100, 1.4 numerical aperture oil-immersion objective and a sCMOS Hamamatsu Ocra Flash camera. A previously described imaging buffer was used to promote proper photoswitching of the Alexa Fluor 647 (10 mM cysteamine MEA (Sigma Aldrich, 30070–50G) in Glox Solution: 0.5 mg $ml^{-1}$ 1-glucose oxidase, 40 mg $ml^{-1}$ 1-catalase (both Sigma) and 10% glucose in PBS)[25,79]. The 640 nm laser (1,000 mW peak power) was used at a setting of 40% to excite the reporter dye (Alexa Fluor 647, Invitrogen) and switch it to the dark state, and the 405 nm laser was gradually increased to reactivate the Alexa Fluor 647 in an activator dye (Alexa Fluor 405)-facilitated manner and maintain a constant density of active fluorophores. The camera exposure time was 15 ms and 30,000 total frames were recorded per image. STORM image localizations were obtained using Nanoimager software (ONI) and rendered with the custom-written software Insight3 (a gift from B. Huang, UCSF, USA)[8]. For quantitative analysis, we used custom-written MATLAB codes. A previously described method that segments super-resolution images based on Voronoi tessellation of the fluorophore localizations was adapted[80,81]. Voronoi tessellation of a STORM image assigns a Voronoi polygon to each localization such that the polygon area is inversely proportional to the local localization density[22]. The spatial distribution of the localization of each nucleus is represented by a set of Voronoi polygons such that the smaller polygon areas correspond to regions of higher density. The nuclear area was calculated by summing all of the Voronoi polygon areas. The Voronoi polygons at the nuclear edge are extremely large and were omitted for all quantifications. Localization density (total number of localizations per nuclear area) of nuclei will vary between different mechanical/chemical treatments. To compare the chromatin organizational changes from different mechanical/

chemical treatments, the localization density of the nuclei should be of similar range. To further address this, the Voronoi polygon area of each nucleus was divided by its mean Voronoi polygon area such that the mean localization density of each nucleus is in reduced units of one. The inverse of a reduced Voronoi polygon area associated with a localization gives the reduced Voronoi density. All reduced Voronoi densities of each nucleus for each category of treatment were pooled and plotted as cumulative distribution plots. A threshold was set such that the first 0–40 percentile of the Voronoi density distribution was assigned to sparse chromatin and the remaining 41–80 percentile was assigned to dense chromatin. Domains were segmented by grouping adjacent Voronoi polygons with areas less than a selected threshold and imposing a minimum of three localizations per domain criteria to generate the final segmented dataset. The border and inside of the nucleus were cropped using a custom-made macro in ImageJ.

### Statistical analyses.

Statistical analyses were performed using Student *t*-tests or ANOVA with Tukey's honestly significantly different post-hoc tests (SYSTAT v.13 and GraphPad Prism v.9). Results are expressed as the mean ± s.d.

### Reporting summary.

Further information on research design is available in the Nature Research Reporting Summary linked to this article.

## Extended Data

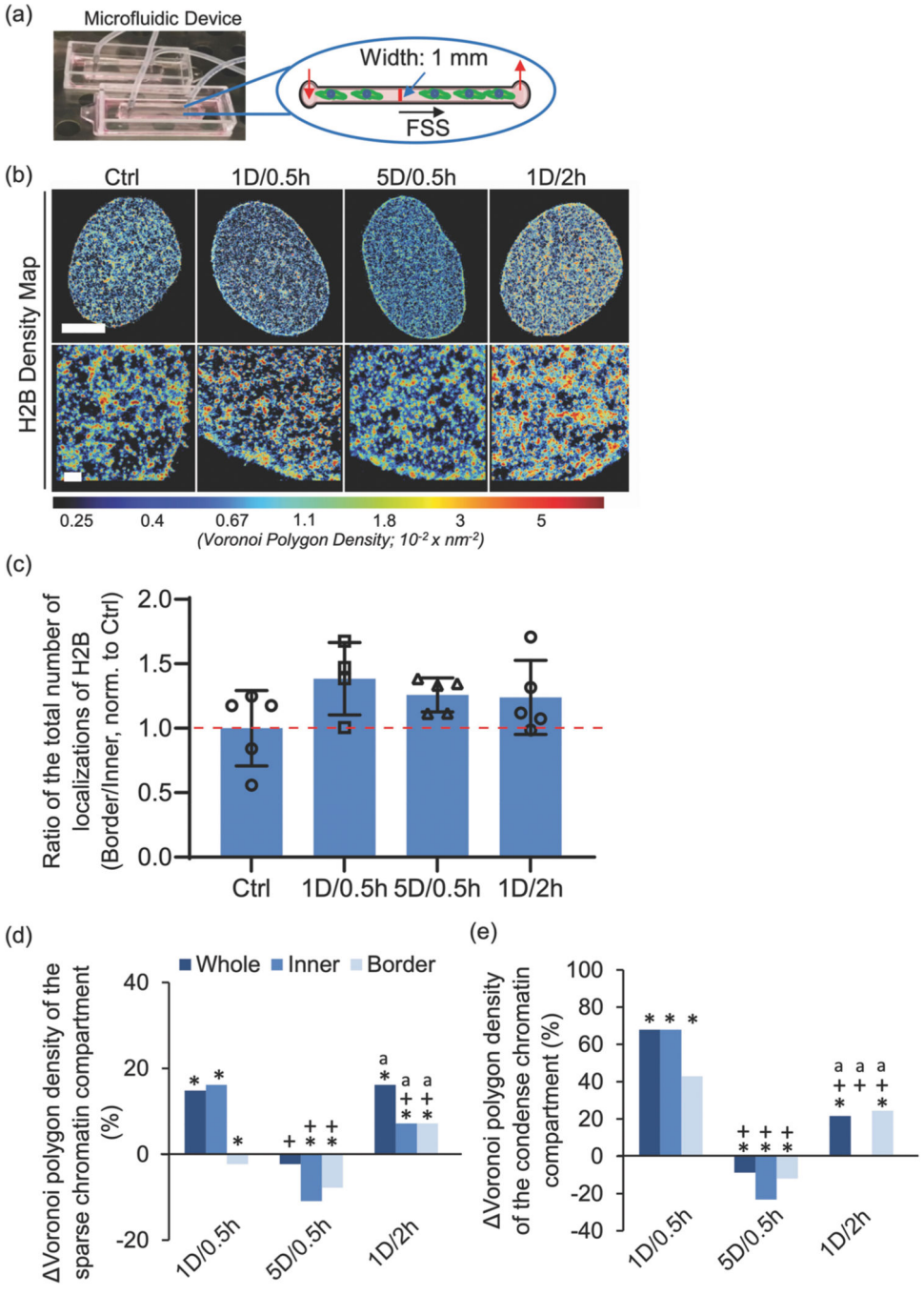


**Extended Data Fig. 1 |. Custom-PdMS microfluidic chamber, and changes in chromatin distribution.**

(**a**) Picture and schematic of a custom-PDMS microfluidic fluid shear stress (FSS) device. (**b**) Representative STORM super-resolution images of H2B rendered as a density map showing redistribution of H2B in hMSCs in response to FSS of varying magnitude 1 ~ 5 dyne/cm$^2$) and duration (0.5 ~ 2 h). (**c**) Quantification of changes in the ratio of the total number of H2B localizations per unit area at the nuclear border to the total number of H2B

localizations at the inner part of the nucleus with/without the application of FSS (*: $p < 0.05$ vs. Ctrl, +: $p < 0.05$ vs. 1D/0.5 h, a: $p < 0.05$ vs. 5D/0.5 h). The values have been normalized to Ctrl cells. (**d**) Changes in chromatin condensation with the application of FSS in (d) sparse chromatin compartment or (**e**) dense chromatin compartment in hMSCs. The Voronoi polygon density of the dense or the sparse chromatin compartment in cells subjected to FSS is shown normalized to the Voronoi polygon density in the absence of FSS ($n = 5$ nuclei/group, *: $p < 0.001$ vs. Ctrl, +: $p < 0.001$ vs. 1D/0.5 h, a: $p < 0.001$ vs. 5D/0.5 h, one-way ANOVA). Experiments were carried out at least in duplicate. Error bars, means ± s.d.

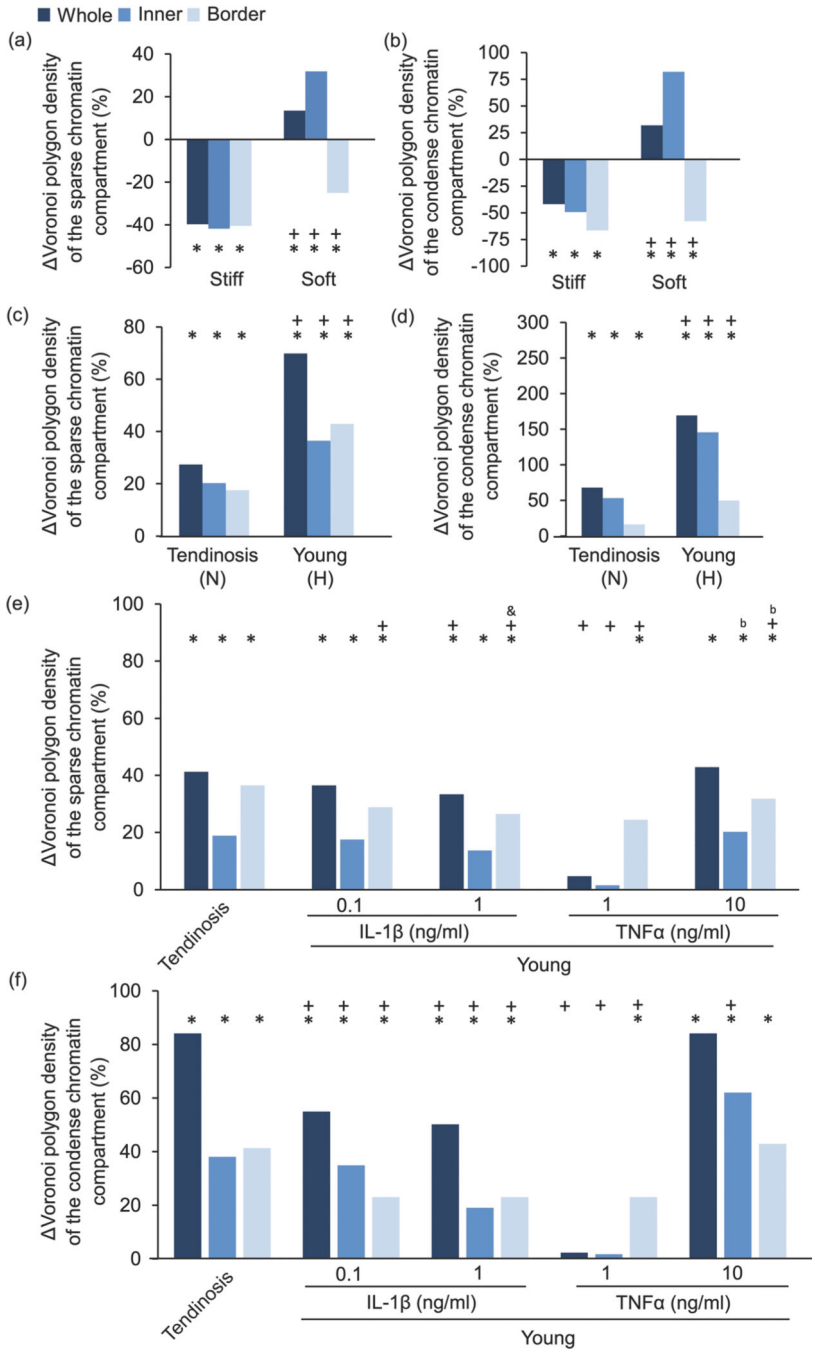


**Extended Data Fig. 2 |. Changes in chromatin condensation with substrate stiffness in sparse chromatin or dense chromatin compartments.**

a,b, The Voronoi polygon density of the sparse (a) or dense (b) chromatin compartment is shown normalized to the Voronoi polygon density in human tenocytes grown on Glass, showing a decrease/increase in the condensation of dense chromatin compartment on stiff/soft substrates (n = 5 nuclei/group, *: $p < 0.001$ vs. glass, +: $p < 0.001$ vs. soft, one-way ANOVA). Changes in chromatin condensation in sparse chromatin (c) or dense chromatin (d) compartments. The Voronoi polygon density of the sparse or dense chromatin compartment is shown normalized to the Voronoi polygon density in human young tenocytes

grown under normoxic (N) conditions, showing an increase in the condensation of dense chromatin under hypoxic (H) conditions (n = 5 nuclei/group, *: $p < 0.001$ vs. young healthy tenocyte under the normoxic conditions, +: $p < 0.001$ vs. tendinosis tenocyte under the normoxic conditions, one-way ANOVA). Changes in chromatin condensation with exposure to inflammatory cytokines in sparse chromatin (e) or dense chromatin (f) compartments. The Voronoi polygon density of the sparse or dense chromatin compartment is shown normalized to the Voronoi polygon density in human young tenocytes without treatment with inflammatory cytokines, showing an increase in the condensation of dense chromatin upon treatment (n = 5 nuclei/group, *: $p < 0.001$ vs. young human tenocyte control, +: $p < 0.001$ vs. tendinosis young human tenocyte, One-way ANOVA). Error bars, means ± s.d.

## Supplementary Material

Refer to Web version on PubMed Central for supplementary material.

## Acknowledgements

The authors thank K.H. Song for assistance with the design of the microfluidic chamber, E. Sorokina for assistance with the preparation of reagents for STORM imaging and P. K. Relich for help with data visualization and analysis tools. The research was funded by the National Institutes of Health (grant no. K01 AR07787 to S-J.H.), Penn Center for Musculoskeletal Disorders (grant no. P30 AR069619 to S-J.H, M.L. and R.L.M.), Department of Veterans Affairs (grant no. IK6 RX003416 to R.L.M.), R01 GM133842 (to M.L.), U01DA052715 (to M.L.) and NSF Science and Technology Center for Engineering Mechanobiology (grant no. CMMI-1548571 to M.L., R.L.M and V.S.). The theoretical work was supported by National Cancer Institute Awards R01CA232256 and U54CA261694; National Institute of Biomedical Imaging and Bioengineering Awards R01EB017753 and R01EB030876; and NSF Grants MRSEC/DMR-1720530 and DMS-1953572.

## Data availability

The authors declare that the main data supporting the findings in this study are available within the paper and its Supplementary Information. The raw STORM super-resolution data files are too large to be publicly shared but are available for research purposes from the corresponding authors on reasonable request. Source data are provided with this paper.

## References

1. Humphrey JD, Dufresne ER & Schwartz MA Mechanotransduction and extracellular matrix homeostasis. Nat. Rev. Mol. Cell Biol 15, 802–812 (2014). [PubMed: 25355505]
2. Wang N, Tytell JD & Ingber DE Mechanotransduction at a distance: mechanically coupling the extracellular matrix with the nucleus. Nat. Rev. Mol. Cell Biol 10, 75–82 (2009). [PubMed: 19197334]
3. Makris EA, Hadidi P. & Athanasiou KA The knee meniscus: structure–function, pathophysiology, current repair techniques, and prospects for regeneration. Biomaterials 32, 7411–7431 (2011). [PubMed: 21764438]
4. Snedeker JG & Foolen J. Tendon injury and repair—a perspective on the basic mechanisms of tendon disease and future clinical therapy. Acta Biomater. 63, 18–36 (2017). [PubMed: 28867648]
5. Han WM et al. Microstructural heterogeneity directs micromechanics and mechanobiology in native and engineered fibrocartilage. Nat. Materials 10.1038/nmat4520 (2016).
6. Tsai SL, Nödl MT & Galloway JL Bringing tendon biology to heel: leveraging mechanisms of tendon development, healing, and regeneration to advance therapeutic strategies. Dev. Dyn 250, 393–413 (2021). [PubMed: 33169466]

7. Klemm SL, Shipony Z. & Greenleaf WJ Chromatin accessibility and the regulatory epigenome. Nat. Rev. Genet 20, 207–220 (2019). [PubMed: 30675018]
8. Ricci MA, Manzo C, García-Parajo MF, Lakadamyali M. & Cosma MP Chromatin fibers are formed by heterogeneous groups of nucleosomes in vivo. Cell 160, 1145–1158 (2015). [PubMed: 25768910]
9. Walker CJ et al. Nuclear mechanosensing drives chromatin remodelling in persistently activated fibroblasts. Nat. Biomed. Eng 10.1038/s41551-021-00709-w (2021).
10. Heo SJ et al. Mechanically induced chromatin condensation requires cellular contractility in mesenchymal stem cells. Biophys. J 111, 864–874 (2016). [PubMed: 27558729]
11. Heo SJ et al. Differentiation alters stem cell nuclear architecture, mechanics, and mechano-sensitivity. eLife 5, e18207 (2016).
12. Le HQ et al. Mechanical regulation of transcription controls Polycomb-mediated gene silencing during lineage commitment. Nat. Cell Biol 18, 864–875 (2016). [PubMed: 27398909]
13. Nava MM et al. Heterochromatin-driven nuclear softening protects the genome against mechanical stress-induced damage. Cell 181, 800–817.e22 (2020).
14. Stephens AD et al. Physicochemical mechanotransduction alters nuclear shape and mechanics via heterochromatin formation. Mol. Biol. Cell 30, 2320–2330 (2019). [PubMed: 31365328]
15. Lakadamyali M. & Cosma MP Visualizing the genome in high resolution challenges our textbook understanding. Nat. Methods 10.1038/s41592-020-0758-3(20DOI20).
16. Ma H. & Liu Y. Super-resolution localization microscopy: toward high throughput, high quality, and low cost. APL Photonics 5, 060902 (2020).
17. Xu J. et al. Super-resolution imaging reveals the evolution of higher-order chromatin folding in early carcinogenesis. Nat. Commun 10.1038/s41467-020-15718-7 (2020).
18. Finnamore E. et al. Transverse tendon stiffness is reduced in people with Achilles tendinopathy: a cross-sectional study. PLoS ONE 10.1371/journal.pone.0211863 (2019).
19. McBeath R. et al. Tendinosis develops from age- and oxygen tension-dependent modulation of Rac1 activity. Aging Cell 18, e12934 (2019).
20. Shah RR, Nerurkar NL, Wang CC & Galloway JL Tensile properties of craniofacial tendons in the mature and aged zebrafish. J. Orthop. Res 33, 867–873 (2015). [PubMed: 25665155]
21. Cho NS, Hwang JH, Lee YT & Chae SW Tendinosis-like histologic and molecular changes of the Achilles tendon to repetitive stress: a pilot study in rats. Clin. Orthop. Relat. Res 469, 3172–3180 (2011). [PubMed: 21800208]
22. Otterstrom J. et al. Super-resolution microscopy reveals how histone tail acetylation affects DNA compaction within nucleosomes in vivo. Nucleic Acids Res. 10.1093/nar/gkz593 (2019).
23. Heinz KS et al. Peripheral re-localization of constitutive heterochromatin advances its replication timing and impairs maintenance of silencing marks. Nucleic Acids Res. 46, 6112–6128 (2018). [PubMed: 29750270]
24. Shaklai S, Amariglio N, Rechavi G. & Simon AJ Gene silencing at the nuclear periphery. FEBS J. 274, 1383–1392 (2007). [PubMed: 17489096]
25. Heo SJ et al. Nuclear softening expedites interstitial cell migration in fibrous networks and dense connective tissues. Sci. Adv 10.1126/sciadv.aax5083 (2020).
26. Kieffer-Kwon KR et al. Myc regulates chromatin decompaction and nuclear Architecture during B cell activation. Mol. Cell 10.1016/j.molcel.2017.07.013 (2017).
27. Neguembor MV et al. Transcription-mediated supercoiling regulates genome folding and loop formation. Mol. Cell 81, 3065–3081 (2021). [PubMed: 34297911]
28. Engler AJ, Sen S, Sweeney HL & Discher DE Matrix elasticity directs stem cell lineage specification. Cell 126, 677–689 (2006). [PubMed: 16923388]
29. Killaars AR et al. Extended exposure to stiff microenvironments leads to persistent chromatin remodeling in human mesenchymal stem cells. Adv. Sci. (Weinh) 6, 1801483 (2019).
30. LaCroix AS, Duenwald-Kuehl SE, Lakes RS & Vanderby R. Relationship between tendon stiffness and failure: a metaanalysis. J. Appl. Physiol 115, 43–51 (2013). [PubMed: 23599401]
31. Handorf AM, Zhou Y, Halanski MA & Li WJ Tissue stiffness dictates development, homeostasis, and disease progression. Organogenesis 11, 1–15 (2015). [PubMed: 25915734]

32. Cosgrove BD et al. N-cadherin adhesive interactions modulate matrix mechanosensing and fate commitment of mesenchymal stem cells. Nat. Mater 15, 1297–1306 (2016). [PubMed: 27525568]
33. Bannister AJ & Kouzarides T. Regulation of chromatin by histone modifications. Cell Res. 21, 381–395 (2011). [PubMed: 21321607]
34. Bártová E, Krejcí J, Harničarová A, Galiová G. & Kozubek S. Histone modifications and nuclear architecture: a review. J. Histochem. Cytochem 10.1369/jhc.2008.951251 (2008).
35. Venkatesh S. & Workman JL Histone exchange, chromatin structure and the regulation of transcription. Nat. Rev. Mol. Cell Biol 16, 178–189 (2015). [PubMed: 25650798]
36. Liu X. et al. Distinct features of H3K4me3 and H3K27me3 chromatin domains in pre-implantation embryos. Nature 10.1038/nature19362 (2016).
37. Akkers RC et al. A Hierarchy of H3K4me3 and H3K27me3 acquisition in spatial gene regulation in xenopus embryos. Dev. Cell 17, 425–434 (2009). [PubMed: 19758566]
38. Gan L. et al. Epigenetic regulation of cancer progression by EZH2: From biological insights to therapeutic potential. Biomark. Res 10.1186/s40364-018-0122-2 (2018).
39. Dudakovic A. et al. Epigenetic control of skeletal development by the histone methyltransferase Ezh2. J. Biol. Chem 10.1074/jbc.M115.672345 (2015).
40. Heo S-J et al. Biophysical regulation of chromatin architecture instills a mechanical memory in mesenchymal stem cells. Sci. Rep 5, 16895 (2015).
41. Sato T. et al. Transcriptional selectivity of epigenetic therapy in cancer. Cancer Res. 10.1158/0008-5472.CAN-16-0834 (2017).
42. Liu Y-B et al. LPA induces osteoblast differentiation through interplay of two receptors: LPA1 and LPA4. J. Cell. Biochem 10.1002/jcb.22471 (2010).
43. Toews ML, Ustinova EE & Schultz HD Lysophosphatidic acid enhances contractility of isolated airway smooth muscle. J. Appl. Physiol 83, 1216–1222 (1997). [PubMed: 9338431]
44. Voorhees PW The theory of Ostwald ripening. J. Stat. Phys 38, 231–252 (1985).
45. Guvendiren M. & Burdick JA Stiffening hydrogels to probe short- and long-term cellular responses to dynamic mechanics. Nat. Commun 10.1038/ncomms1792 (2012).
46. Caliari SR et al. Stiffening hydrogels for investigating the dynamics of hepatic stellate cell mechanotransduction during myofibroblast activation. Sci. Rep 6, 21387 (2016).
47. Dakin SG et al. Inflammation activation and resolution in human tendon disease. Sci. Transl. Med 7, 311ra173 (2015).
48. Tempfer H. & Traweger A. Tendon vasculature in health and disease. Front. Physiol 6, 330 (2015). [PubMed: 26635616]
49. Millar NL et al. Hypoxia: a critical regulator of early human tendinopathy. Ann. Rheum. Dis 71, 302–310 (2012). [PubMed: 21972243]
50. John T. et al. Effect of pro-inflammatory and immunoregulatory cytokines on human tenocytes. J. Orthop. Res 28, 1071–1077 (2010). [PubMed: 20127972]
51. Mobasheri A. & Shakibaei M. Is tendinitis an inflammatory disease initiated and driven by pro-inflammatory cytokines such as interleukin 1β? Histol. Histopathol 28, 955–964 (2013). [PubMed: 23463583]
52. Svensson RB, Heinemeier KM, Couppé C, Kjaer M. & Magnusson SP Effect of aging and exercise on the tendon. J. App. Physiol 121, 1237–1246 (2016).
53. Turan A, Teber MA, Yakut ZI, Unlu HA & Hekimoglu B. Sonoelastographic assessment of the age-related changes of the Achilles tendon. Med. Ultrasonography 17, 58–61 (2015).
54. Arya S. & Kulig K. Tendinopathy alters mechanical and material properties of the Achilles tendon. J. Appl. Physiol 108, 670–675 (2010). [PubMed: 19892931]
55. Arvind V. & Huang AH Reparative and maladaptive inflammation in tendon healing. Front. Bioeng. Biotechnol 9, 719047 (2021).
56. Schulze-Tanzil G. et al. The role of pro-inflammatory and immunoregulatory cytokines in tendon healing and rupture: new insights. Scand. J. Med. Sci. Sports 21, 337–351 (2011). [PubMed: 21210861]
57. Mirabella AC, Foster BM & Bartke T. Chromatin deregulation in disease. Chromosoma 125, 75–93 (2016). [PubMed: 26188466]

58. Zoghbi HY & Beaudet AL Epigenetics and human disease. Cold Spring Harb. Persp. Biol 8, a019497 (2016).
59. Saul D. & Kosinsky RL Epigenetics of aging and aging-associated diseases. Int. J. Mol. Sci 22, 401 (2021). [PubMed: 33401659]
60. Gnan S, Liu Y, Spagnuolo M. & Chen C-L The impact of transcription-mediated replication stress on genome instability and human disease. Genome Instab. Dis 1, 207–234 (2020).
61. Strom AR et al. Phase separation drives heterochromatin domain formation. Nature 547, 241–245 (2017). [PubMed: 28636597]
62. Becker JS et al. Genomic and proteomic resolution of heterochromatin and its restriction of alternate fate genes. Mol. Cell 10.1016/j.molcel.2017.11.030 (2017).
63. van Steensel B. & Belmont AS Lamina-associated domains: links with chromosome architecture, heterochromatin, and gene repression. Cell 169, 780–791 (2017). [PubMed: 28525751]
64. Bitman-Lotan E. & Orian A. Nuclear organization and regulation of the differentiated state. Cell. Mol. Life Sci 10.1007/s00018-020-03731-4 (2021).
65. Yao L, Bestwick CS, Bestwick LA, Maffulli N. & Aspden RM Phenotypic drift in human tenocyte culture. Tissue Eng. 12, 1843–1849 (2006). [PubMed: 16889514]
66. Gardner OFW, Alini M. & Stoddart MJ Mesenchymal stem cells derived from human bone marrow. Methods Molec. Biol 1340, 41–52 (2015). [PubMed: 26445829]
67. Loebel C, Mauck RL & Burdick JA Local nascent protein deposition and remodelling guide mesenchymal stromal cell mechanosensing and fate in three-dimensional hydrogels. Nat. Mater 10.1038/s41563-019-0307-6 (2019).
68. Song KH et al. Influence of fiber stiffness on meniscal cell migration into dense fibrous networks. Adv. Healthc. Mater 10.1002/adhm.201901228 (2020).
69. Davidson MD et al. Engineered fibrous networks to investigate the influence of fiber mechanics on myofibroblast differentiation. ACS Biomater. Sci. Eng 5, 3899–3908 (2019). [PubMed: 33438429]
70. Sagui C. & Desai RC Ostwald ripening in systems with competing interactions. Phys. Rev. Lett 74, 1119–1122 (1995). [PubMed: 10058939]
71. Cahn JW & Hilliard JE Free energy of a nonuniform system. I. Interfacial free energy. The J. Chem. Phys 28, 258 (1958).
72. Zwicker D, Hyman AA & Jülicher F. Suppression of Ostwald ripening in active emulsions. Phys. Rev. E 92, 012317 (2015).
73. Poleshko A. et al. Genome-nuclear lamina interactions regulate cardiac stem cell lineage restriction. Cell 171, 573–587 (2017). [PubMed: 29033129]
74. Buchwalter A, Kaneshiro JM & Hetzer MW Coaching from the sidelines: the nuclear periphery in genome regulation. Nat. Rev. Genet 20, 39–50 (2019). [PubMed: 30356165]
75. Towbin BD, Gonzalez-Sandoval A. & Gasser SM Mechanisms of heterochromatin subnuclear localization. Trends Biochem. Sci 38, 356–363 (2013). [PubMed: 23746617]
76. Glotzer SC, Stauffer D. & Jan N. Glotzer, Stauffer, and Jan reply. Phys. Rev. Lett 75, 1675 (1995). [PubMed: 10060358]
77. Christensen JJ, Elder K. & Fogedby HC Phase segregation dynamics of a chemically reactive binary mixture. Phys. Rev. E 54, R2212–R2215 (1996).
78. Alisafaei F, Jokhun DS, Shivashankar GV & Shenoy VB Regulation of nuclear architecture, mechanics, and nucleocytoplasmic shuttling of epigenetic factors by cell geometric constraints. Proc. Natl Acad. Sci. USA 116, 13200–13209 (2019).
79. Cella Zanacchi F. et al. A DNA origami platform for quantifying protein copy number in super-resolution. Nat. Methods 14, 789–792 (2017). [PubMed: 28650478]
80. Andronov L, Orlov I, Lutz Y, Vonesch JL & Klaholz BP ClusterViSu, a method for clustering of protein complexes by Voronoi tessellation in super-resolution microscopy. Sci. Rep 6, 24084 (2016).
81. Levet F. et al. SR-Tesseler: a method to segment and quantify localization-based super-resolution microscopy data. Nat. Methods 10.1038/nmeth.3579 (2015).

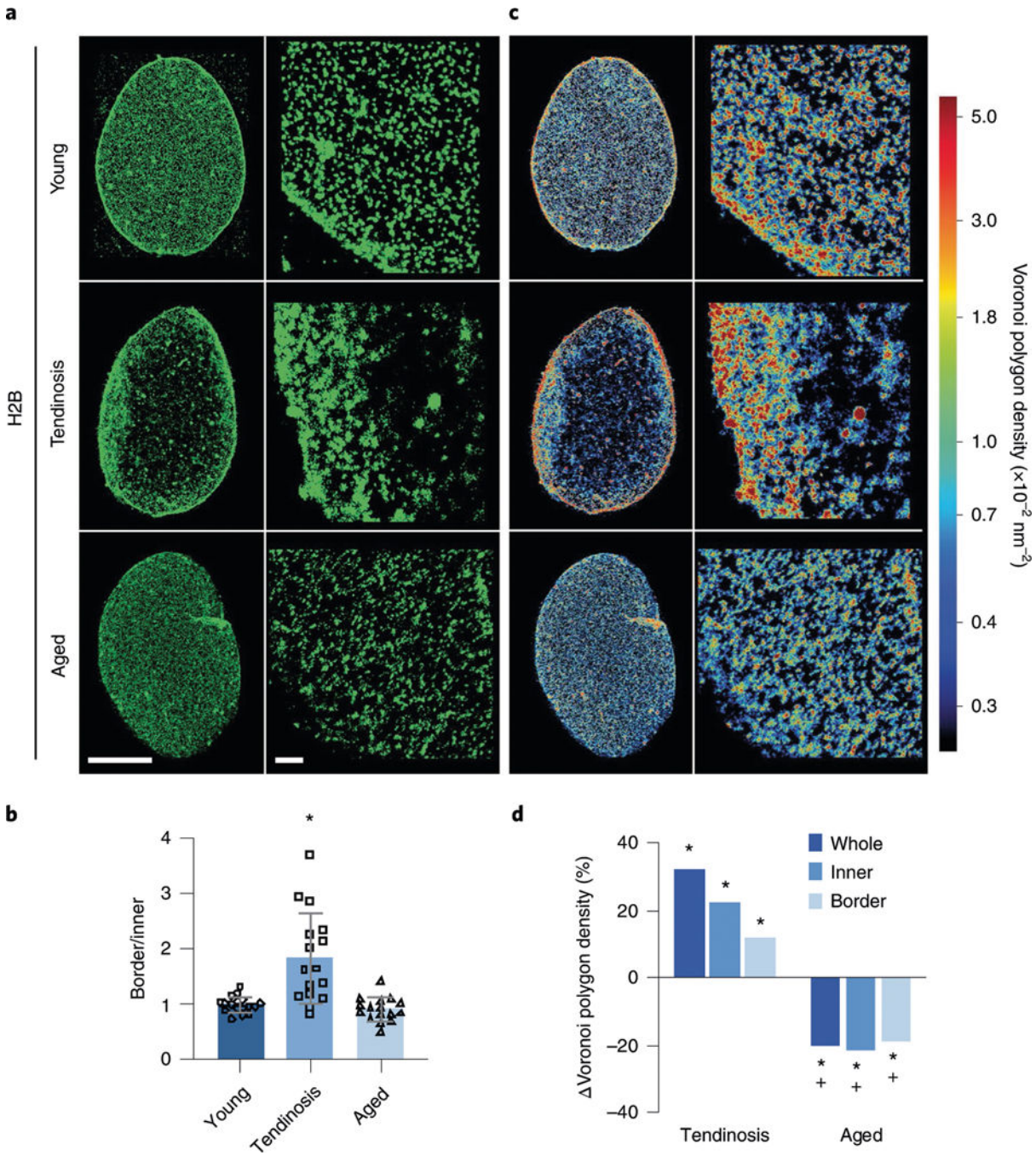


**Fig. 1 |. Altered nanoscale H2B localization in hTCs with degeneration.**

**a**, Representative STORM super-resolution images of H2B. Scale bars, 5 μm (left) and 300 nm (right). **b**, Ratio of the total number of H2B localizations per unit area at the nuclear border to the total number of H2B localizations in the inner region of the nucleus. The values were normalized to those of young and healthy cells. H2B was labelled with primary and secondary antibodies, and STORM super-resolution images of H2B were obtained using the photo-switchable Alexa Fluor 647 dye conjugated to the secondary antibody. Localizations correspond to individual detections of the Alexa Fluor 647 in the STORM

super-resolution images of H2B and the total number of localizations is proportional to (but due to the variable labelling stoichiometry and repeated fluorophore blinking, not equal to) the total number of H2B proteins ($n \approx 16$ nuclei per group from two biological replicates; $*P < 0.001$ versus young, one-way analysis of variance (ANOVA)). **c**, STORM super-resolution images of H2B from **a** rendered as Voronoi density maps based on Voronoi tessellation of H2B localizations showing disease and ageing-dependent changes to the spatial localization and compaction of the chromatin. Voronoi polygons were colour-coded according to their area, with red corresponding to small Voronoi polygons (that is, high H2B density) and blue corresponding to large Voronoi polygons (that is, low H2B density). **d**, Changes in chromatin condensation in the dense chromatin compartment (which corresponds to the 41–80th percentile of the cumulative Voronoi polygon density plot averaged over multiple hTC nuclei) of hTCs from young, tendinosis and aged donors. The Voronoi polygon density of the dense chromatin compartment was normalized to the Voronoi polygon density in hTCs obtained from the young and healthy donor ($n \approx 16$ nuclei per group from two biological replicates; $*P < 0.001$ versus young, $^{+}P < 0.001$ versus tendinosis, one-way ANOVA). The experiments were carried out at least three times. Data are the mean ± s.d.

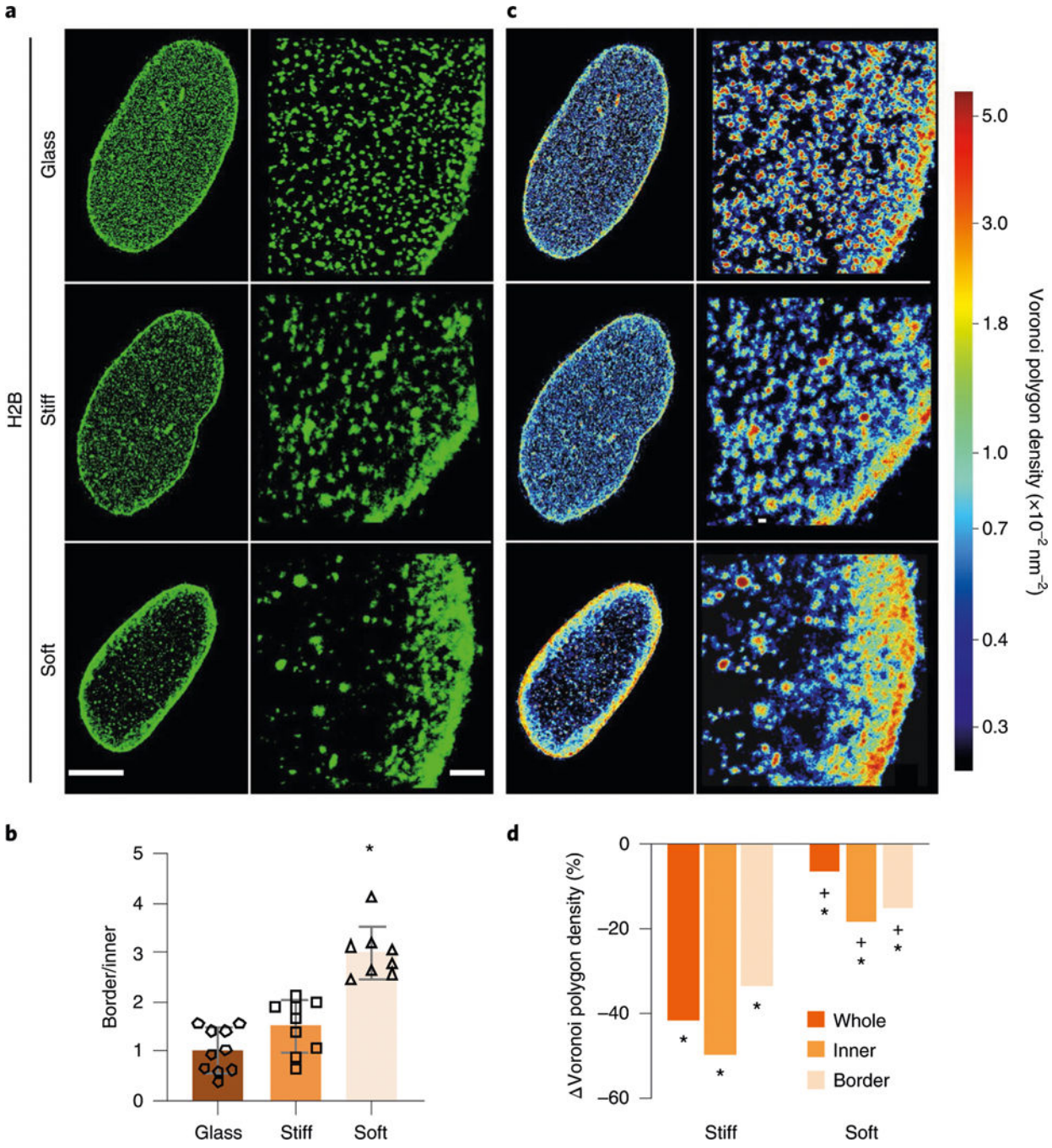


**Fig. 2 |. Substrate stiffness regulates H2B localizations in hMSCs.**

**a**, Representative STORM super-resolution images of H2B in hMSCs cultured on glass, and stiff and soft hydrogels. Scale bars, 5 μm (left) and 300 nm (right). **b**, Ratio of the total number of H2B localizations per unit area at the nuclear border to the total number of H2B localizations in the inner region of the nucleus. The values were normalized to those for the glass substrate ($n \approx 9$ nuclei per group; $^*P < 0.001$ versus both glass and stiff, one-way ANOVA). **c**, STORM super-resolution images of H2B from **a** rendered as a Voronoi density map based on Voronoi tessellation of H2B localizations showing substrate-dependent

changes to the spatial localization and compaction of the chromatin. Voronoi polygons were colour-coded according to their area, with red corresponding to small Voronoi polygons (that is, high H2B density) and blue corresponding to large Voronoi polygons (that is, low H2B density). **d**, Changes in chromatin condensation in the dense chromatin compartment of the nuclei of hMSCs on different substrates. The Voronoi polygon density of the dense chromatin compartment was normalized to the Voronoi polygon density in hMSCs on glass substrate ($n \approx 9$ nuclei per group, $^{*}P < 0.001$ versus glass, $^{+}P < 0.001$ versus stiff, one-way ANOVA). The experiments were carried out at least three times. Data are the mean ± s.d.

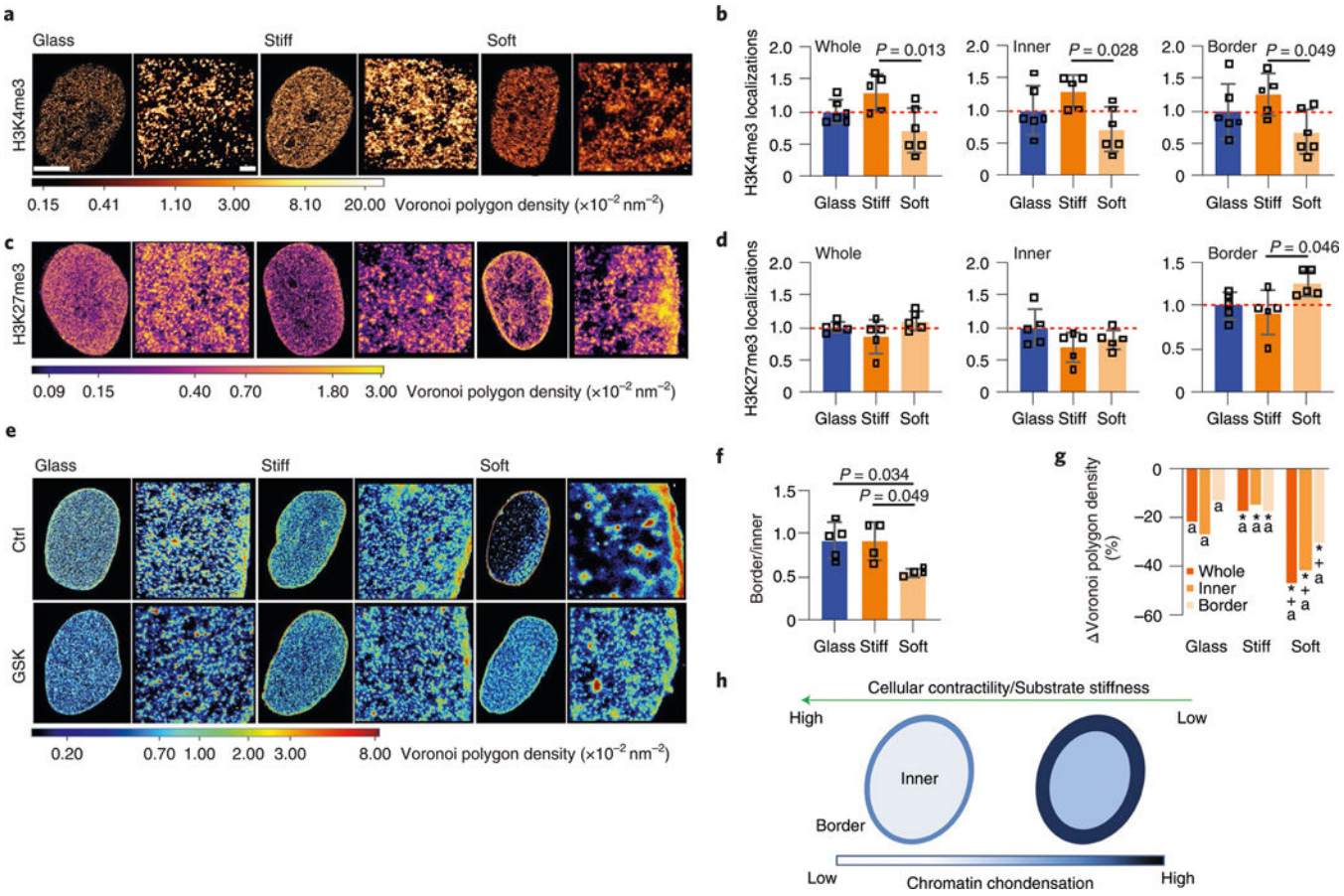


**Fig. 3 |. Substrate-stiffness-dependent histone methylation in hMSCs.**

**a**,**c**, Representative STORM super-resolution images of H3K4me3 (**a**) and H3K27me3 (**c**) rendered as a density map based on the Voronoi polygon density, with yellow corresponding to high Voronoi polygon density and black corresponding to low Voronoi polygon density showing the nanoscale spatial distribution of histone methylation in hMSCs on different substrates (glass and stiff or soft MeHA hydrogels). Scale bars, 5 μm (main images; left) and 300 nm (magnified views; right). **b**,**d**, Total number of H3K4me3 (**b**; $n = 5$ nuclei per group) and H3K27me3 (**d**; $n = 5$ (glass and stiff) and 6 (soft) nuclei) localizations per unit area on the whole, border or inner region of the hMSC nucleus on different substrates. The values were normalized to those for the glass substrate and the normalized value for the glass substrate is shown as a red dashed line drawn at 1. **e**, Representative STORM super-resolution images of H2B rendered as a density map based on Voronoi polygon density, with red corresponding to high Voronoi polygon density and blue corresponding to low Voronoi polygon density, in the nuclei of hMSCs on different substrates (glass or stiff and soft MeHA hydrogels) with or without GSK343 (GSK) treatment. **f**, Changes to H2B localization between the nuclear border and inner region of nuclei with and without GSK treatment quantified as the ratio of the number of localizations of H2B per unit area at the nuclear border to the total number of localizations of H2B per unit area at the inner region of the nucleus. The values shown are for GSK treatment, which were further normalized to the control group. **b**,**d**,**f**, *P* values were determined using a one-way ANOVA.

**g**, Changes to the condensation level of the dense chromatin compartment in GSK-treated hMSCs compared with control hMSCs. The Voronoi polygon density of the dense chromatin compartment in GSK-treated hMSCs was normalized to control hMSCs; a decrease in chromatin condensation of dense chromatin compartment with GSK treatment was observed ($^{a}P < 0.001$ versus control, $^{*}P < 0.001$ versus glass and $^{+}P < 0.001$ versus stiff; two-way ANOVA). **f**,**g**, $n = 5$ (glass control and GSK, and soft control) and 4 (stiff control and GSK, and soft GSK) nuclei. The experiments were carried out at least twice. Data are the mean ± s.d. **h**, Schematic showing that substrate stiffness regulates nanoscale spatial chromatin organization and condensation mediated by histone methylation in hMSCs (yellow circles, H2Bs; red arrows, H2B relocalization to the nuclear border).

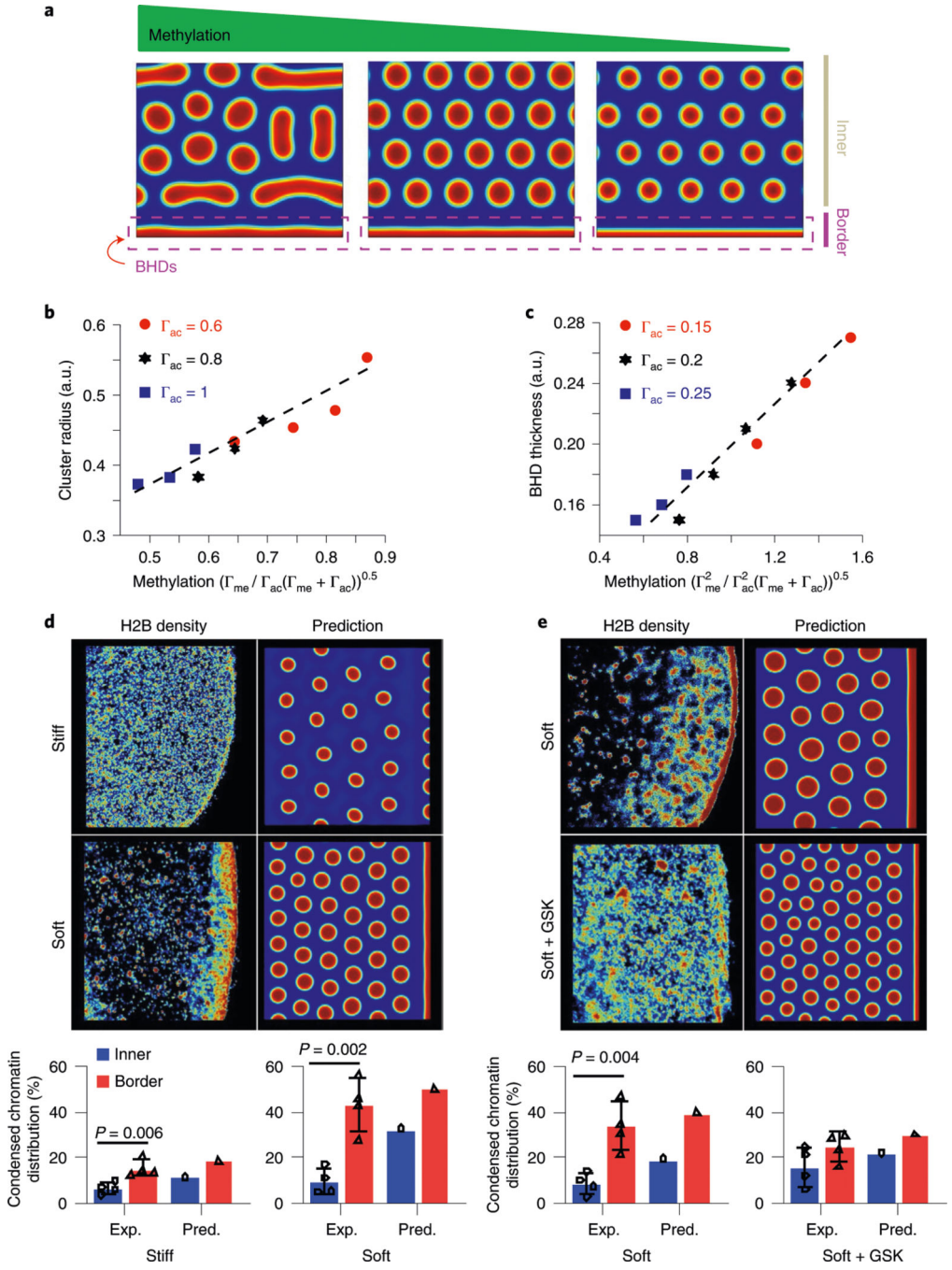


**Fig. 4 |. A phase-field model of heterochromatin formation incorporating the kinetics of acetylation and methylation recapitulates experimental results.**

**a**, Impact of increasing methylation on the organization of chromatin. Blue and red represent euchromatin-rich and heterochromatin-rich phases, respectively. **b**, Scaling relationship between the size of heterochromatin cluster (a.u.) with the level of methylation. **c**, Scaling relationship between the thickness of nuclear border (a.u.) heterochromatin domains (BHDs) with the level of methylation. **d**, Experimental measurements and model predictions of heterochromatin percentage at the nuclear border and interior for cells cultured on either

soft or stiff substrates. Images on the left correspond to experimental STORM images of H2B color coded according to Voronoi polygon size as in previous figures. The images on the right correspond to model predictions showing euchromatin in blue and heterochromatin in red. Plots show the percentage of chromatin at the nuclear border (red) and interior (blue) calculated from the STORM images of H2B (Exp.) and from the model predictions (Pred.). **e**, Experimental measurements and model predictions of heterochromatin percentage at the nuclear border and interior for cells treated with or without GSK343 cultured on soft substrates. Images on the left correspond to experimental STORM images of H2B color coded according to Voronoi polygon size as in previous figures. The images on the right correspond to model predictions showing euchromatin in blue and heterochromatin in red. Plots show the percentage of chromatin at the nuclear border (red) and interior (blue) calculated from the STORM images of H2B (Exp.) and from the model predictions (Pred.). **d**,**e**, Exp., experiment; pred., predicted. *P* values were determined using a double-sided Student's *t*-test; $n = 4$. Data are the mean ± s.d.

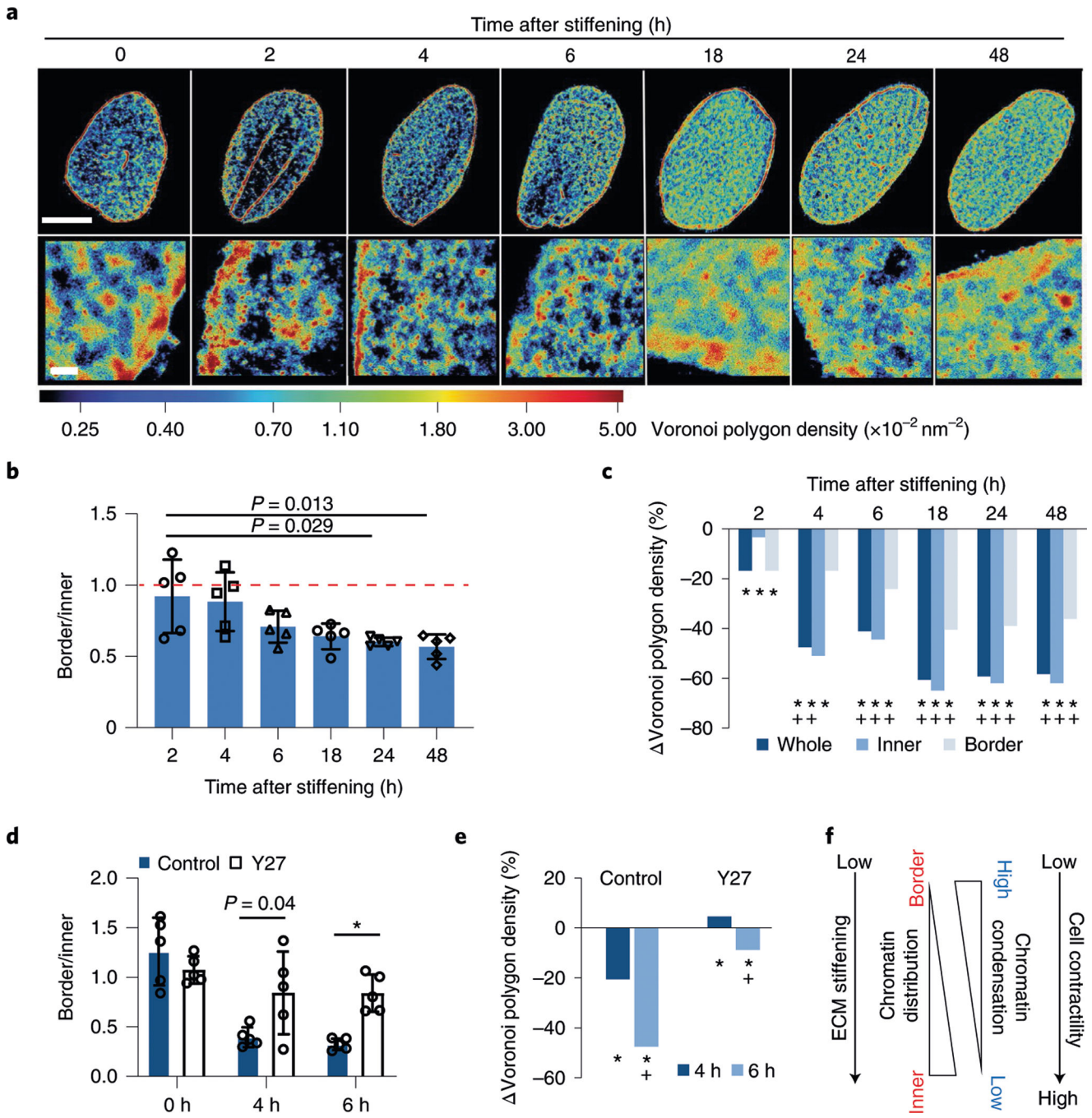


**Fig. 5 |. effect of in situ stiffening on nanoscale chromatin organization in hMSCs.**

**a**, Representative STORM super-resolution images of H2B rendered as a Voronoi polygon density map showing a continual redistribution of H2B from the nuclear periphery to the nuclear interior 0–48 h after stiffening. Scale bars, 5 μm (top) and 300 nm (bottom). **b**, Ratio of the total number of localizations of H2B at the nuclear border to the total number of localizations of H2B in the inner region of the nucleus. The values were normalized to the starting value at 0 h ($n = 5$ nuclei per group; $P$ values were determined using a one-way ANOVA). Red dashed line is set at 1 corresponding to the normalized starting value at 0 h.

**c**, Changes in chromatin condensation in the dense chromatin compartment in hMSCs 0–48 h after stiffening. The Voronoi polygon density of the dense chromatin compartment in cells cultured on the stiffening hydrogel was normalized to the starting Voronoi polygon density at 0 h, showing a decrease in chromatin condensation of dense chromatin with time after stiffening ($n = 5$ nuclei per group; $^{*}P < 0.0001$ versus 0 h, $^{+}P < 0.001$ versus 2 h, one-way ANOVA). **d**, Ratio of the total number of localizations of H2B per unit area at the nuclear border to the total number of localizations of H2B at the inner part of the nucleus for hMSCs cultured on stiffening hydrogel with/without Y27 treatment at different times after stiffening, showing that Y27 prevents the relocalization of chromatin from the nuclear border to the nuclear interior following stiffening ($n = 5$ nuclei per group; $^{*}P < 0.001$ versus 0 h, double-sided Student's *t*-test). **e**, Changes in chromatin condensation in condensed dense chromatin compartment in hMSCs cultured on the stiffening hydrogel with/without Y27 treatment. Y27 treatment prevents a decrease in chromatin condensation of dense chromatin with time after stiffening. The Voronoi polygon density of the condensed dense chromatin compartment in cells cultured on the stiffening hydrogel with or without Y27 treatment was normalized to the starting Voronoi polygon density at 0 h ($n = 5$ nuclei per group; $^{*}P < 0.0001$ versus 0 h, $^{+}P < 0.001$ versus 4 h, two-way ANOVA). **f**, Schematic showing how ECM stiffening regulates chromatin distribution and condensation in hMSCs through actomyosin-based cellular contractility. ECM stiffening redistributes chromatin from the border to the inner region of the hMSC nucleus, resulting in chromatin decondensation, which requires cellular contractility. The experiments were carried out at least three times. Data are the mean ± s.d.

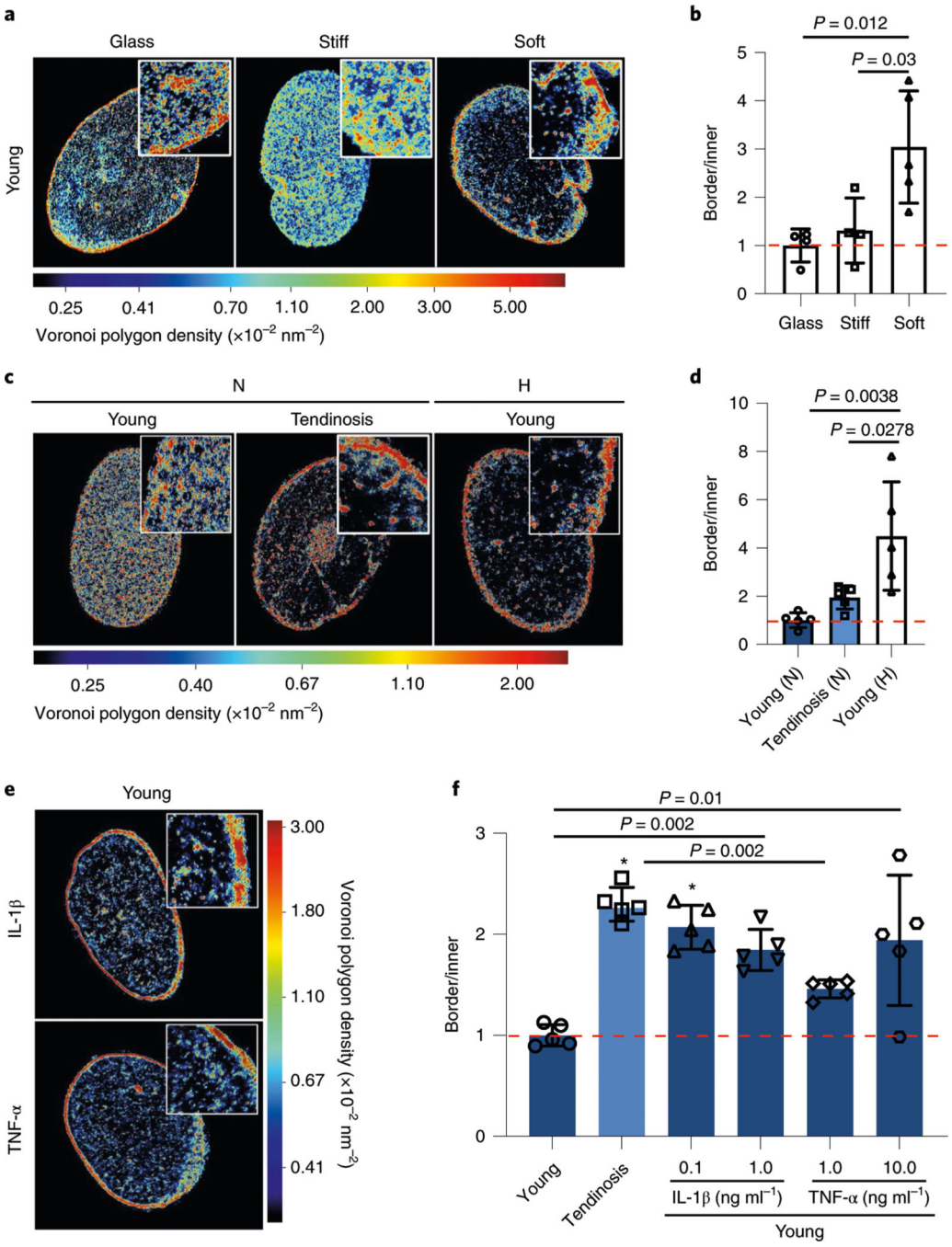


**Fig. 6 |. Altered nanoscale H2B localization in hTCs with presentation of degenerative chemophysical cues.**

**a**, Representative STORM super-resolution images of H2B rendered as a density map showing changes to H2B localization in hTCs cultured on different substrates. **b**, Ratio of the total number of H2B localizations per unit area at the nuclear border to the total number of H2B localizations in the inner region of the nucleus, showing relocalization of H2B to the nuclear border in hTCs cultured on soft substrates. The values were normalized to those for the glass substrate. **c**, Representative STORM super-resolution images of H2B

rendered as a Voronoi polygon density map showing changes to H2B localization in young and tendinosis hTCs under normoxic conditions, and young hTCs under hypoxic conditions. **d**, Ratio of the total number of H2B localizations per unit area at the nuclear border to the total number of H2B localizations in the inner region of the nucleus, showing relocalization of H2B to the nuclear border in young hTCs under hypoxic conditions. The values were normalized to those of young hTCs cultured under normoxic conditions. **b**,**d**, Red dashed line is set at 1, the normalized value for hTCs grown on glass (**b**) or young hTCs under normoxic conditions (**d**). *P* values were determined using a one-way ANOVA; $n = 5$ nuclei per group. **c**,**d**, N, normoxia; and H, hypoxia. **e**, Representative STORM super-resolution images of H2B rendered as a Voronoi polygon density, showing changes to H2B localization in hTCs cultured on glass substrates with or without exposure to IL-1β (1 ng $ml^{-1}$; top) and TNF-α (10 ng $ml^{-1}$; bottom). **f**, Ratio of the total number of H2B localizations per unit area at the nuclear border to the total number of H2B localizations in the inner region of the nucleus, showing relocalization of H2B to the nuclear border following treatment with inflammatory cytokines. The values were normalized to those of the young hTC control without exposure to IL-1β or TNF-α ($n = 5$ nuclei per group; $*P < 0.001$ versus young hTC control, one-way ANOVA). Red dashed line is set at 1, the normalized value for hTC control without exposure to IL-1β or TNF-α. **a**,**c**,**e**, Scale bars, 5 μm (main images) and 300 nm (insets). The experiments were carried out at least two times. Data are the mean ± s.d.

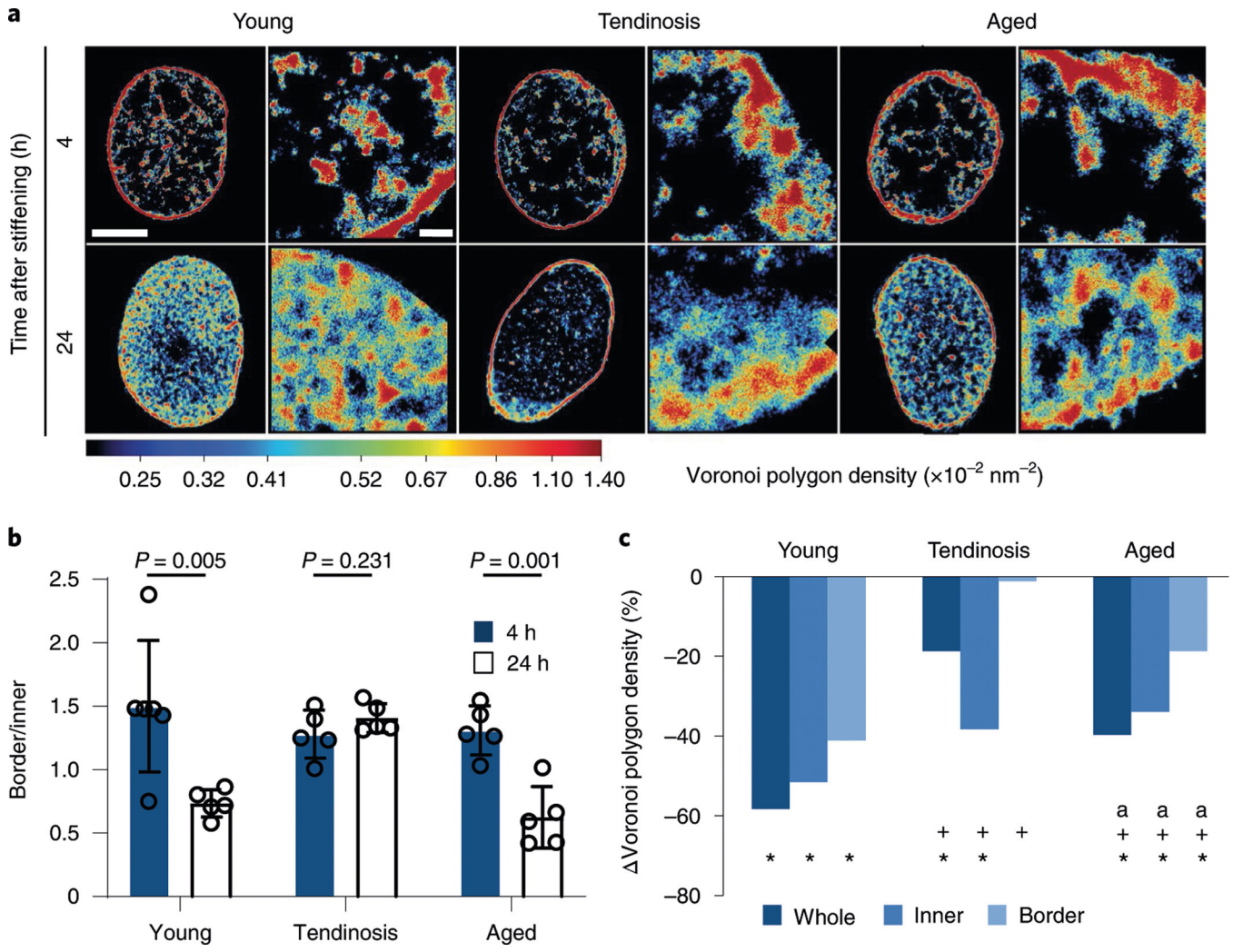


**Fig. 7 |. Altered mechanical sensitivity of hTCs with tissue degeneration and ageing.**

**a**, Representative STORM super-resolution images of H2B rendered as a density map showing changes to H2B localization in young, tendinosis and aged hTCs 4 and 24 h after stiffening. **b**, Ratio of the total number of H2B localizations per unit area at the nuclear border to the total number of H2B localizations in the inner region of the nucleus, showing a lack of response in the relocalization of H2B to the nuclear interior after stiffening in tendinosis hTCs ($n = 5$; $P$ values were determined using a double-sided Student's $t$-test). **c**, Changes in chromatin condensation in the dense chromatin compartment 24 h after stiffening. The Voronoi polygon density of the dense chromatin compartment was normalized to the Voronoi polygon density 4 h after stiffening ($n = 5$ nuclei per group; $^{*}P < 0.001$ versus 4 h, $^{+}P < 0.001$ versus young and $^{a}P < 0.001$ versus tendinosis; one-way ANOVA). The experiments were carried out at least two times. Data are the mean ± s.d.

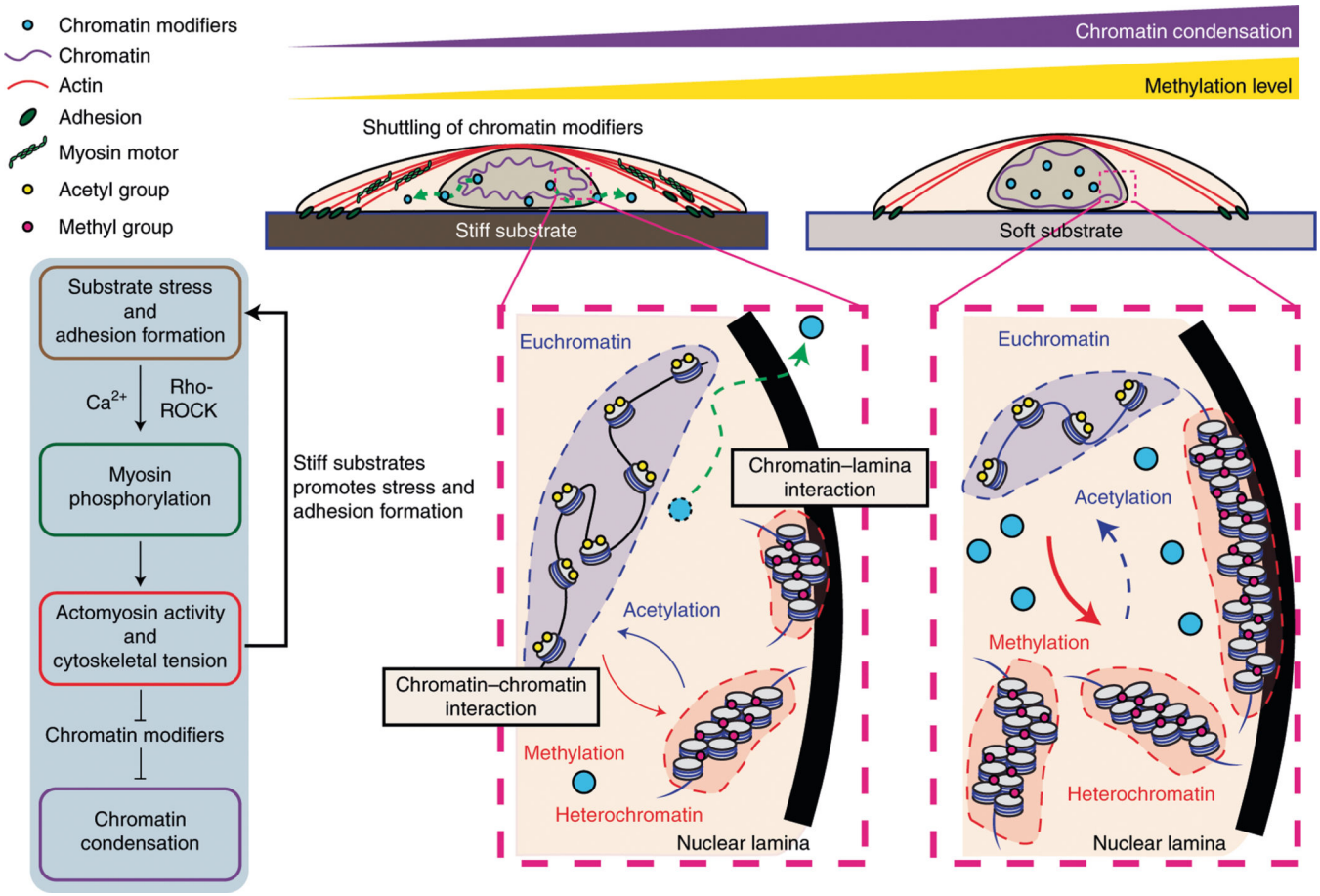


**Fig. 8 |. Proposed model for how substrate stiffness alters nanoscale chromatin organization, mediated by changes in cellular contractility or Rho–RoCK pathways and mechano-activation and nuclear localization of chromatin modifiers.**

Higher stiffness of the substrate alters actomyosin-based cellular contractility, thereby promoting the formation of actin stress fibres and focal adhesion, and regulating the shuttling of chromatin modifiers (for example, HDAC and EZH2) into or out of the nucleus. These epigenetic modifiers alter the nanoscale chromatin spatial organization and condensation via regulation of histone acetylation/methylation levels.